Fuel 409 (2026) 137820

Contents lists available at ScienceDirect

Fuel

journal homepage: www.elsevier.com/locate/fuel

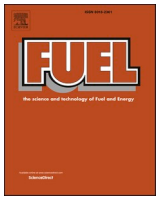

Full Length Article

Hydrogen storage performance of porous carbons from waste Cotton: Activation strategies, isotherm and kinetic analyses

Mecit Karadaş [a], Gözde Duman [b], Mehmet Doğan [a,*], Yasemin Turhan [a], Tamer Karayıldırım [b]

[a] Balikesir University, Faculty of Science and Literature, Department of Chemistry, 10145 Çağış-Balıkesir, TURKEY
[b] Ege University, Faculty of Science, Department of Chemistry, Bornova-İzmir, Türkiye

ARTICLE INFO

Keywords:
Pyrolysis
Biomass
Biochar
Hydrogen storage
Isotherm
Kinetics

ABSTRACT

In this study, biomass-based carbon materials with high surface area were synthesized from cotton waste via different activation techniques for hydrogen storage applications. The effects of key process parameters—including pyrolysis temperatures (300–800 °C), activation agent ratios (KOH/biomass = 1:10 or 1:20), and activation atmospheres (N_2 and CO_2)—were systematically investigated. Characterization was performed using BET, FTIR, DTA/TG and SEM/EDX analyses. The highest surface area (1446 m^2/g) and micropore volume (0.570 cc/g) were obtained for the sample pyrolyzed at 800 °C and activated under CO_2 flow with KOH/biomass impregnation ratio of 1:10, resulting in a highly porous structure. Hydrogen adsorption experiments at 77 K and 17.4 bar revealed a maximum storage capacity of 2.79 wt% for the optimized carbon material, surpassing the theoretical prediction of Chahine's rule. Adsorption isotherms were best described by the Langmuir model ($R2 > 0.996$), indicating monolayer coverage on a homogeneous surface. Kinetic modeling showed that the pseudo-second-order model best fit the experimental data. Additionally, Weber–Morris model demonstrated that intra-particle diffusion influenced the adsorption mechanism. Correlation analysis confirmed strong relationships between hydrogen storage capacity and both BET surface area ($R = 0.87$) and micropore volume ($R = 0.86$). These results highlight the potential of cotton-derived porous carbon material as low-cost, sustainable, and effective adsorbents for hydrogen storage systems. Importantly, the study demonstrates that combining chemical (KOH) and physical (CO_2) activation enables the production of high–surface-area carbons while substantially reducing KOH usage, representing a key novelty and a more sustainable alternative to traditional activation approaches.

1. Introduction

Nowadays, the depletion of fossil fuels and the increasing environmental issues have intensified interest in alternative energy sources, with hydrogen energy emerging as a sustainable solution. Hydrogen provides approximately 33 kWh/kg of gravimetric energy density—three times more than fossil fuels—and offers zero-emission potential by releasing only water vapor as a byproduct of combustion [1,2]. The fact that it can be produced from water and renewable sources further strengthens hydrogen's central role in a sustainable energy cycle [3]. However, one of the main obstacles to the widespread use of hydrogen energy is the lack of sufficiently developed safe, efficient, and cost-effective storage and transportation methods. Hydrogen can be stored as a gas under high pressure, as a liquid at low temperatures, or through physical/chemical adsorption on solid surfaces. Although gas-phase storage offers advantages such as quick access and low cost, the need for high pressure poses safety risks. Liquid-phase storage, on the other hand, provides higher energy density but is limited by the high energy consumption required for extreme cooling [3,4]. In contrast, hydrogen storage using solid adsorbents offers safer storage conditions at lower operating pressures and can achieve high hydrogen adsorption capacities due to their typically high surface areas. In this context, porous and lightweight carbon-based adsorbents such as carbon nanotubes [5], fullerenes [6], activated carbons [7], and graphene-based materials [8] have gained prominence in hydrogen storage research. The hydrogen storage capacity of multi-walled carbon nanotubes (MWCNTs) has been investigated under various temperature and pressure conditions. While the storage capacity of pristine MWCNTs was measured to be 2.02 wt%

* Corresponding author.
E-mail address: mdogan@balikesir.edu.tr (M. Doğan).

https://doi.org/10.1016/j.fuel.2025.137820
Received 19 September 2025; Received in revised form 18 November 2025; Accepted 30 November 2025
Available online 2 December 2025

at 77 K, chemical modification increased the capacity of MWCNT-COCl to 3.17 wt% [9]. The hydrogen storage capacity of defective fullerenes has been determined as 2.17 wt% at 77 K. Experimental results indicate that hydrogen molecules are adsorbed onto both the internal and external surfaces of fullerenes via van der Waals forces. Furthermore, it has been observed that defective fullerene structures are more effective in storing hydrogen [10]. The hydrogen storage capacity of activated carbon derived from chestnut shells was measured to be 3.18 wt% at 77 K. These results suggest that activated carbon may serve as an effective storage material due to its high surface area and micropore volume [7]. The hydrogen storage capacity of lithium-doped graphene was determined to be 1.416 wt% at 298 K and 1.605 wt% at 77 K. Additionally, the surface area of graphene was reported to be 689 m^2/g, which facilitates more efficient hydrogen adsorption [8]. However, it is evident that the hydrogen storage capacities of these materials generally remain low. These findings highlight the need for the development of environmentally friendly, novel carbon-based materials and further investigation into their hydrogen storage capabilities.

In recent years, extensive research has focused on producing adsorbents with high surface area and enhanced pore structures through the carbonization of plant-based waste biomass using various methods. In this context, the hydrogen storage performance of carbons derived from different biomass sources has been widely investigated in the literature. For instance, carbon produced from waste coffee grounds via KOH activation exhibited a surface area of 2070 m^2/g and a high micropore volume, with hydrogen storage capacities of 0.6 wt% at 298 K and 4.0 wt % at 77 K [10]. Carbons obtained from olive leaves using microwave and chemical methods showed a 13 % improvement in hydrogen storage capacity after ultrasonic treatment due to enhanced pore structure [1]. Moreover, it has been demonstrated that hydrogen adsorption is closely related to surface area and pore structure, particularly in studies conducted on carbon materials with cylindrical pore structures [11]. An optimized activated carbon derived from date seeds presented a surface area of 846.7 m^2/g [12]. Due to their high crystalline cellulose content, cotton fibers can produce carbon structures with higher carbon yield and well-developed narrow micropores (<2 nm) during pyrolysis and activation [13]. In addition, their intrinsic fibrous and channel-like morphology facilitates the propagation of pores along the fiber direction during activation, resulting in highly interconnected micro/mesoporous networks with large specific surface area [14]. Moreover, the cellulose-to-carbon conversion pathway, including aromatic framework formation and micropore development, has been well-documented in the literature [15]. Therefore, cotton waste offers distinct advantages over many other biomass precursors, combining structural suitability for micropore generation with low cost, wide availability, and sustainability. Various porous carbon derivatives have also been produced from cotton-based biomass. Examples include biomorphic carbon from cotton stalks [16], ultra-high surface area carbons [17], chemically activated carbons [18], and carbonized structures derived from lignin [19]. Physical activation, particularly using CO_2, typically results in porous carbon with relatively low surface area or adequete porosity is achived by high activation temperatures and prolonged durations [20].On the other hand, chemical activation methods such as KOH or $ZnCl_2$ yield significantly higher surface areas but involve corrosive reagents [21]. Recently, combining both physical and chemical activation has emerged as a promising approach to enhance porosity while reducing the required amount of chemical agents. Patel et al. (2023) activated pine saw dust via carbonization followed by KOH (biomass:KOH ratio of 1:2) activation, CO_2 activation and their combination [22]. The combined activation resulted in a higher surface area (2216 m^2/g) compared to KOH (1319 m^2/g) and CO_2 (336 m^2/g) activation alone. Although many studies have reported porous carbons derived from different biomass sources, systematic evaluations of hydrogen storage performance in cotton-waste–derived biochars under varying activation routes remain limited. In this study, the key novelty lies in the systematic comparison of chemical activation (KOH), physical activation (CO_2), and their combined application on cotton waste. The combined activation strategy enables the formation of interconnected narrow micropores while reducing the amount of KOH required, thereby providing a more sustainable and environmentally favorable pathway for producing high-performance porous carbons. We hypothesize that the high cellulose content and fibrous morphology of cotton waste will facilitate the development of narrow micropores (<2 nm) during activation, leading to hydrogen storage capacities comparable to or even higher than those of other biomass-derived carbons. By correlating hydrogen storage capacity with BET surface area and micropore volume, this work establishes a quantitative structure–adsorption relationship specific to cotton-based biochars, demonstrating the combined activation approach as the core innovative contribution of this study. Therefore, the aim of this study is to investigate the hydrogen storage performance of biochars produced from cotton wastes under various pyrolysis and activation conditions through comprehensive characterization, isotherm, and kinetic analyses. In this context, i. the effects of pyrolysis temperature, atmosphere type, KOH ratio, and CO_2 gas flow speed on the properties of the biomass-based carbon materials (CM) were examined, ii. material characterization was performed using Brunner–Emmett–Teller (BET) surface area analysis, Fourier Transform Infrared Spectroscopy (FTIR), Differential Thermal Analysis/Thermogravimetry (DTA/TG), and Scanning Electron Microscopy/Energy Dispersive X-ray Spectroscopy (SEM/EDX), iii. hydrogen storage capacities were compared at both room and cryogenic temperatures, and iv. adsorption behavior was thoroughly evaluated using adsorption isotherm and kinetic models. Additionally, the statistical relationship between hydrogen storage capacity and BET surface area as well as micropore volume was analyzed to quantitatively reveal the correlation between surface–microstructure–adsorption. In this way, the study proposes a novel approach for converting low-cost cotton wastes into high value-added materials for energy-related applications.

2. Materials and methods

2.1. Materials

Cotton wastes were obtained from Izmir, Türkiye. All chemicals used in this study were of analytical grade and were used without further purification.

2.2. Methods

2.2.1. Preparation of biochars

All pyrolysis and activation processes were carried out in a 1 L vertical fixed-bed reactor made of 316 stainless steel. The pyrolysis system has been detailed in a previous studies [21,23]. A total of nine biochars were produced from cotton waste using pyrolysis under various conditions. In pyrolysis experiments, the heating rate (10 °C/min) was selected based on preliminary experiments to ensure controlled carbonization without structural collapse. Activation durations of 1 h and 3 h were chosen to compare moderate and extended activation while preventing excessive burn-off. CO_2 flow rates (25–100 mL/min) were selected to evaluate the effect of gas–solid interaction kinetics on pore development. These conditions are consistent with commonly reported activation parameters for cellulose-based biomass-derived carbons. The production methods are described below. In this study, the raw cotton waste was labeled as P0.

Approximately 30 g of cotton waste was loaded into the reactor. The reactor was then placed inside an external furnace, and the heating rate of the furnace was set to 10 °C/min. Nitrogen gas (N_2) with a flow rate of 100 mL/min was used both as a purge gas and to create an inert atmosphere. The reactor was separately heated to 300 and 800 °C and maintained at these temperatures for 1 h. Subsequently, the reactor was cooled to room temperature under a continuous flow of N_2. The resulting biochar was recovered from the reactor, and the samples obtained at 300

and 800 °C were labeled as P1 and P2, respectively.

KOH activation of the cotton waste was performed using the wet impregnation method. An appropriate amount of KOH was dissolved in approximately 20 mL of water. Then, 20 g of biomass was impregnated with the solution at KOH/biomass ratios of 1:10 and 1:20. The resulting slurry was stirred and subsequently dried in an oven at 105 °C overnight. The dried mixture was then thermally activated in a fixed-bed pyrolysis system at 800 °C for 1 h under a nitrogen flow of 100 mL/min. The residue from the reactor was cooled with 150 mL of 10 % HCl solution for 1 h and filtered under vacuum. The solid was washed with warm distilled water until no chloride ions were detected in the filtrate. The obtained biochars were dried in an oven at 105 °C. The biochar produced at a KOH:biomass ratio of 1:10 was labeled as P4, while that at a ratio of 1:20 was labeled as P5.

For CO_2 activation, the cotton waste was placed in a stainless steel pyrolysis reactor and heated to 800 °C at a rate of 10 °C/min under a nitrogen flow of 100 mL/min. Once the temperature reached 800 °C, the nitrogen flow was switched to carbon dioxide (CO_2) at a flow rate of 100 mL/min for 3 h. At the end of the activation period, the reactor was allowed to cool to room temperature under a continuous nitrogen flow. The biochar activated with CO_2 was labeled as P3.

In this stage of the activation procedure, both KOH and CO_2 activation techniques were integrated. For this purpose, cotton waste was impregnated with an adequate amount of KOH (at KOH/biomass mass ratios of 1:10 and 1:20) dissolved in 20 mL of water, and the mixture was dried overnight at 105 °C. The dried mixture was then heated to 800 °C and activated under a continuous CO_2 flow (at flow rates of 25, 50, and 100 mL/min) for 3 h. The resulting solid was cooled with a 10 % HCl solution for 1 h, filtered, and washed with warm distilled water under vacuum until no chloride ions were detected in the filtrate. Biochars produced with a KOH/biomass ratio of 1:10 at CO_2 flow rates of 25, 50, and 100 mL/min were labeled as P7, P8, and P9, respectively. The biochar produced at a KOH/biomass ratio of 1:20 and a CO_2 flow rate of 100 mL/min was labeled as P6. To prevent any influence of residual inorganic salts on adsorption or hydrogen storage performance in above all experiments, all activated samples were washed in 10 % HCl solution for 1 h to remove possible salts formed during activation. After acid washing, the samples were thoroughly rinsed with deionized hot water until the chloride test was negative, confirming the removal of salt residues.

2.2.2. Hydrogen storage

The hydrogen storage capacities of the biochar samples were determined using a Hiden IMI PSI gas sorption analyzer. Prior to hydrogen adsorption measurements, the samples were degassed at 200 °C for 4 h. Adsorption tests were conducted under both room temperature and cryogenic conditions within a pressure range of 0–100 bar [24]. Approximately 80 ± 5 mg of each sample was used for each adsorption measurement. Before each pressure step, the system was allowed to reach adsorption equilibrium, and the equilibration time was set as the point where the pressure change was less than 0.01 bar within 20 min. Hydrogen uptake values were normalized per gram of adsorbent (wt%). The reported hydrogen storage values correspond to excess adsorption capacity. Hydrogen storage measurements were performed in duplicate, and the variation between repeated measurements was below 5 %, confirming reproducibility.

2.2.3. Characterization

2.2.3.1. BET surface area and pore volume analysis. The BET surface area and pore volume analyses of the raw cotton waste and biochar samples were performed using a Quantachrome Nova 2200e analyzer. Prior to the measurements, the samples were degassed at 200 °C for 4 h. Nitrogen gas was used as the adsorbate, and measurements were conducted at 77 K in a liquid nitrogen environment. The obtained data were used to evaluate the surface area and pore structure of the cotton waste and biochar samples. BET surface area and pore volume measurements were performed in triplicate, and the reported values represent the mean of repeated analyses.

2.2.3.2. FTIR spectra. FTIR analyses were conducted to investigate the structural changes of the raw cotton waste and biochar samples. The spectra were recorded in the wavenumber range of 600–4000 cm^{-1} using a Perkin Elmer Spectrum 100 FTIR spectrometer. Before analysis, the samples were mixed with KBr at a 1 % ratio and pressed into pellets.

2.2.3.3. DTA/TG analysis. Thermal analyses were carried out using a Perkin Elmer Diamond DTA/TG instrument. The samples were analyzed under a nitrogen atmosphere at a heating rate of 20 °C/min over a temperature range of 30–1000 °C. The mass changes over time were recorded, and the resulting thermograms were used to evaluate the thermal behavior of the samples. For the thermal kinetic analysis of sample P9, thermal measurements were performed in the temperature range of 30–1000 °C, at heating rates of 10, 15, 20 and 25 °C/min.

2.2.3.4. SEM/EDX Imaging. Before SEM analysis, the samples were coated with Au/Pd for 90 s under a current of 20 μA to enhance conductivity. SEM images were obtained using a Zeiss EVO LS 10 microscope at an accelerating voltage of 20 kV. Elemental composition analyses were performed using a Bruker EDX detector.

3. Results and discussion

3.1. Characterization

3.1.1. FTIR analysis

FTIR spectra of cotton waste (P0) and pyrolysis samples (P1-P9) are given in Fig. 1. In FTIR analysis, shifts in band positions, increases or decreases in band intensity, formation of new peaks and changes in functional group diversity are important indicators in determining structural changes. Fig. 1a shows the FTIR spectra of cotton waste (P0), biochars pyrolyzed at 300 and 800 °C (P1 and P2) and biochar pyrolyzed at 800 °C in CO_2 atmosphere (P3). Since cotton waste has cellulose content, characteristic bands originating from cellulose and hemicellulose are observed in the FTIR spectrum. The broad and intense band observed at 3447 cm^{-1} is attributed to the stretching vibrations of hydroxyl groups originating from cellulose, hemicellulose and lignin. The width and intensity of this band indicate that the biomass has high hydrophilic properties. The bands at 2925 and 2854 cm^{-1} correspond to the asymmetric C–H and symmetric –CH_2– stretching vibrations of aliphatic chain structures originating from hemicellulose and lignin. The band at 1751 cm^{-1} represents the stretching vibrations of carbonyl groups (C=O), while the stretching vibrations of conjugated C=C bonds and/or –OH vibrations of adsorbed water are observed at 1637 cm^{-1}. The band at 1377 cm^{-1} indicates the –CH bending vibrations originating from lignin and hemicellulose. The band at 1162 cm^{-1} originates from the glycoside bonds (C–O–C stretching; ether bonds or C–O; alcohol/ester) in the crystal structure of cellulose. These findings reveal that the biochar obtained from cotton waste has a rich cellulose and lignin content. In addition, the presence of hydroxyl, carbonyl and aromatic groups in the spectrum was confirmed; this shows that cotton waste is a biomass suitable for processes such as chemical activation and surface modification. The FTIR spectrum of P1 belongs to biochar pyrolyzed at low temperature (300 °C). Although the cellulose structure started to decompose in this sample, the characteristic bands specific to cotton waste were largely preserved. P2 was pyrolyzed at high temperature (800 °C) and it was observed that most of the functional groups disappeared with the effect of increasing temperature and the structure started to carbonize. P3 represents biochar pyrolyzed at 800 °C; it can be said that the functional groups were largely lost in this spectrum and a

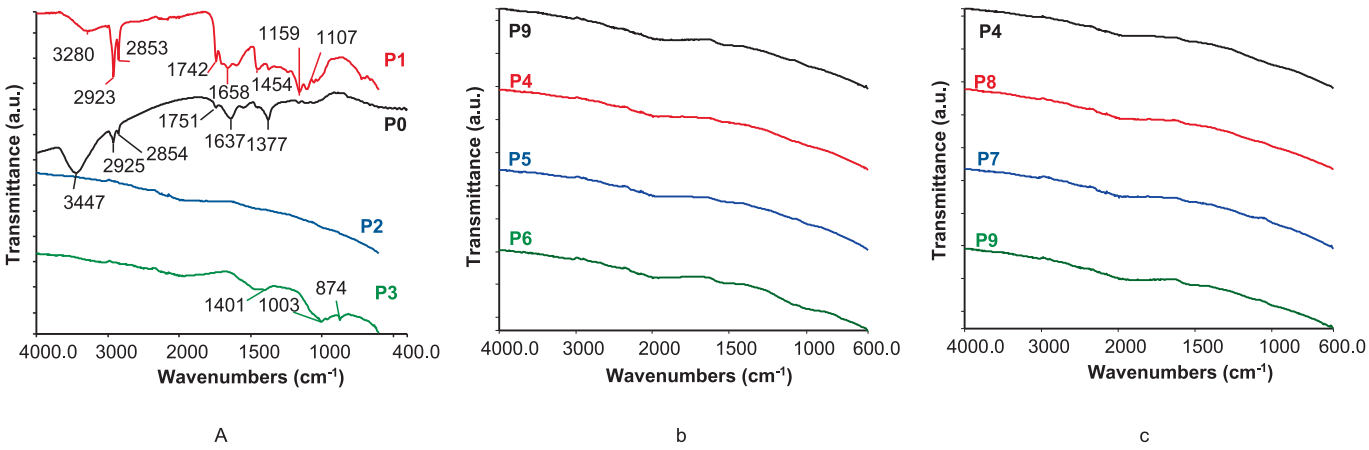

Fig. 1. FTIR spectra of P0-P9 samples.

more porous structure was formed compared to P1 and P2 [18]. The preference of CO_2 atmosphere in the production of activated carbon provides a slower gasification process, controls the reaction of KOH activation agent with carbon and thus allows the formation of more regular and homogeneous pore structures. In addition, since CO_2 provides a mildly oxidizing environment rather than an inert one like nitrogen, it may cause the removal of some functional groups on the surface or their transformation into more stable forms [25]. Fig. 1b shows the FTIR spectra of P4, P5, P6 and P9 biochars. No bands originating from any functional group on the surface were observed. Fig. 1c shows the FTIR spectra of P4, P7, P8 and P9 biochars. No bands are observed in the FTIR spectra for all samples. This shows that the functional groups are completely removed from the surface and a carbon-based structure is formed. During thermal activation of cellulose-based cotton waste with KOH, the functional groups on the surface were removed as a result of the reaction of KOH with carbon to form volatile compounds such as H_2, H_2O and CO_2. This process supported the formation of porous biochar with high surface area [26].

A quantitative comparison of the FTIR spectra clearly demonstrates a systematic structural transformation across the P0 (biomass), P1 (300 °C pyrolyzed), and P9 (activated carbon) samples. In P0, strong O–H, aliphatic C–H, C=O, and C–O–C bands are observed, whereas these functional groups exhibit moderate reductions in P1, decreasing by approximately 14–13 %, consistent with partial dehydration, cleavage of aliphatic chains, and initial decomposition of oxygen-containing groups at low pyrolysis temperatures. The ~ 8 % increase in the aromatic C=C band intensity further indicates the onset of structural condensation and aromatization in P1. In contrast, all characteristic functional group bands disappear entirely in P9, demonstrating 100 % loss of O–H, C–H, C=O, and C–O–C vibrations. This complete removal of functional groups confirms that high-temperature KOH activation leads to full carbonization and the formation of a surface devoid of residual organic functionalities. Overall, the quantitative FTIR evaluation strongly supports the progressive transition from functionalized biomass (P0) to partially carbonized material (P1), and finally to a fully carbonized activated carbon structure (P9).

3.1.2. DTA/TG analysis

Thermogravimetric analysis (TGA) is a crucial technique for examining the thermal behavior and characteristics of biomass, providing valuable insights into energy conversion processes [27]. Fig. 2 presents the DTA/TG thermograms and their derivatives of biochars produced from cotton waste under various conditions. The thermal stability parameters calculated from these thermograms are listed in Table 1. The mass loss steps observed in the TG curves and the peak points in the d[TG] curves offer significant information about the degradation mechanisms of the samples. Raw cotton waste (P0) exhibited a four-stage degradation profile. Low-temperature moisture loss occurs at 82 °C, which corresponds to moisture content removal in biochars between 51 and 87.5 °C. In the intermediate temperature regions, the main pyrolysis step of hemicellulose, cellulose, and lignin ($Tmax_2$=339.0 °C-58.0 wt% and $Tmax_2$=526.3 °C-13.8 wt%), specific to the lignocellulosic structure, and the degradation of carbonaceous structures ($Tmax_2$=963.4 °C-11.9 wt%) were observed. At the end of the analysis at 1000 °C, the

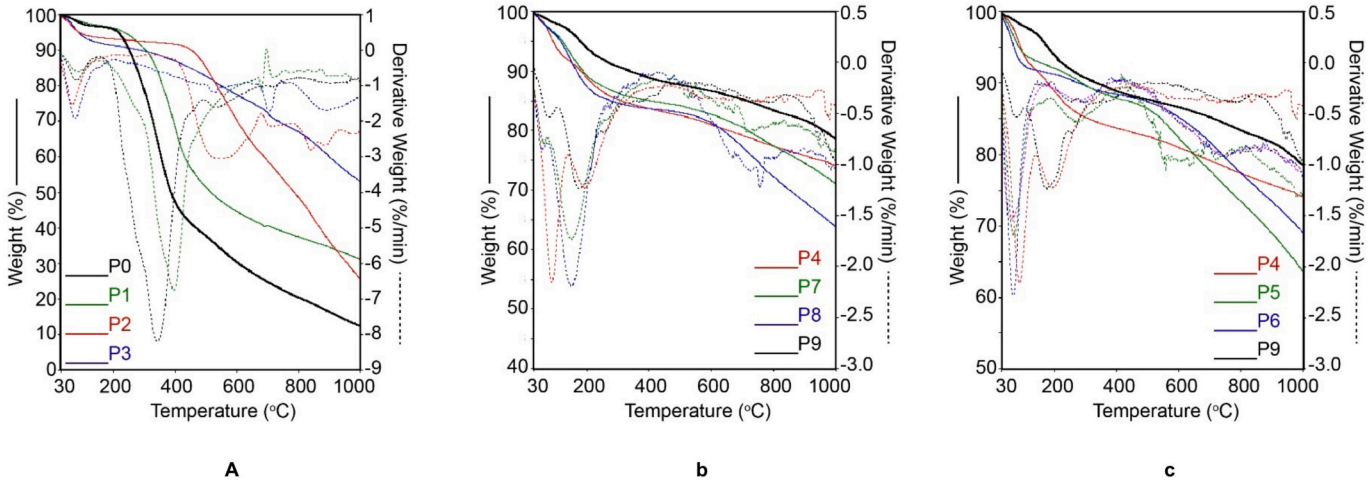

Fig. 2. TG and d[TG] thermograms of a) P0, P1, P2 and P3, b) P4, P7, P8 and P9 and c) P4, P5, P6 and P9.

Table 1
Thermal stability parameters of cotton waste and biochars.

Samples	$Tmax_1$	ΔY_1	$Tmax_2$	ΔY_2	$Tmax_3$	ΔY_3	$Tmax_4$	ΔY_4	Residue at 1000 °C (%)
P0	82.0	3.4	339.0	58.0	526	13.8	963.4	11.9	12.3
P1	85.4	2.7	395.6	53.6	869.6	7.8	–	–	31.1
P2	65.2	6.8	547.4	32.1	834.1	34.4	–	–	25.6
P3	74.4	8.8	523.8	15.7	707.8	7.3	895.6	14.8	53.1
P4	88.2	8.2	195.1	8.7	980.9	8.8	–	–	74.1
P5	73.9	7.5	404.4	4.6	551.9	23.9	–	–	63.6
P6	68.7	7.9	292.4	3.1	861.4	13.4	–	–	69.0
P7	64.0	2.1	146.6	13.0	990.9	13.5	–	–	71.0
P8	51.0	2.8	166.5	13.9	757.7	19.7	–	–	63.7
P9	85.4	1.7	171.2	7.3	769.4	5.4	–	–	78.5
P9 (10 °C)	63.9	2.1	146.7	11.1	743.7	5.6	–	–	77.3
P9 (15 °C)	72.7	2.4	168.0	10.4	758.6	5.0	–	–	78.3
P9 (25 °C)	80.0	1.6	181.9	10.6	778.9	5.3	–	–	80.2

remaining material P0 showed a mass loss of 3.5 wt%. In samples P1 and P2, obtained by heat treatment at 300 °C and 800 °C in an inert atmosphere, it was observed that the amount of volatile matter decreased with increasing temperature, the degree of carbonization increased, and consequently, the Tmax values increased significantly. Sample P3, produced with CO_2 activation, exhibited lower $Tmax_2$ values compared to P2, indicating that the carbon skeleton became more reactive due to the mild oxidizing nature of CO_2. In samples P4 and P5, which underwent chemical activation, $Tmax_2$ values decreased significantly due to the aggressive degradation of the cellulosic structure by KOH. With increasing KOH/biomass ratio, the degradation became more gradual, and higher ash accumulation occurred. This indicates that volatile components decreased in the pyrolyzed samples and a more stable structure was formed. Hemicellulose generally decomposes between 200 and 350 °C, while cellulose decomposes between 250 and 450 °C. In general, with the degradation of hemicellulose, light volatile organic compounds such as water vapor, carbon dioxide (CO_2), methanol and acetic acid are removed from the structure; with the degradation of cellulose, highly volatile compounds, tar and gaseous products are removed; with the degradation of lignin, complex products such as phenolic compounds, fixed carbon, CO_2, CH_4 and aromatic structures are removed from the structure [28–32]. Lignin is known to decompose in the range of 300–600 °C and at a lower rate [29]. In samples P6–P9, where KOH and CO_2 activation were applied together, it was determined that the thermal behavior became more complex, and low $Tmax_2$ values reflected the dense porous and weakened carbon structure created by chemical and gas-phase activation, while high residue percentages indicated that the remaining mineral content in the structure after activation increased. It was observed that increasing the CO_2 flow rate (especially in the P9 series) resulted in increased reactivity by carving out the carbonaceous structure to a greater extent, while an inorganic residue structure resistant to degradation at high temperatures became dominant. Generally speaking, biochars pyrolyzed at high temperatures in an inert atmosphere exhibited the highest thermal stability, while samples using KOH and CO_2 together (especially in P9) exhibited the most intense activation degree, the lowest $Tmax_2$ values, and the highest residue amounts, clearly demonstrating that activation methods have a strong and decisive effect on the thermal behavior of biochar. Furthermore, slow mass losses in TG thermograms and broad peaks in d[TG] thermograms are characteristic. This slow decomposition was particularly evident in P3. The third and fourth degradation steps in the d[TG] thermograms of P3 indicate oxidative decomposition of fixed carbon at high temperatures. The $Tmax_3$ and $Tmax_4$ values in P6 were measured as 707.8 °C and 895.6 °C, respectively, and these samples exhibited high-temperature resistance, indicating that advanced carbonization occurred and that the decomposition of fixed carbon took a long time. The TG/d[TG] thermograms in Fig. 2 also support these table data. As seen in Fig. 2a, the fastest mass loss among P0, P1, P2, and P3 was observed in P0, while these losses were determined to occur slower in the higher temperature range in the biochar samples. P4, P5, P6, P7, P8, and P9 in Fig. 2b and c tend to decompose slower and leave high residue. The d[TG] peak observed between 600–800 °C can be attributed to the decomposition of carbonates and/or excessive gasification of carbon. Based on the data above, the high fixed carbon content and increased thermal stability of the resulting biochars enable their use not only for hydrogen storage but also as potential carbon sources for other applications requiring high thermal resistance, such as flame retardants and electrode materials for fuel cells. Thus, these biomass-based materials contribute to multifunctional applications.

In the literature, various non-isothermal kinetic methods have been developed to determine thermal kinetic analysis parameters by examining the relationships between reaction maximum temperatures and heating rates, with the Kissinger and Ozawa methods being the most well-known and widely used methods [33,34]. The the Kissinger-Akahira-Sunose (KAS) method, considered an isoconversional form of the Kissinger approach, offers a model-independent procedure derived from the differential-derivative form of Arrhenius kinetics. In this method, the reaction mechanism is assumed to be unchanged for a given transformation degree (α), eliminating the need for an explicit definition of the transformation function. The KAS equation provides a linear expression that allows the activation energy to be determined depending on the transformation using data obtained at different heating rates [35]. According to the KAS Eq. (1), the relationship between the heating rate β, the maximum decomposition temperature T, the pre-exponential factor A, the gas constant R, and the activation energy E_a takes a linear form. The slope of the line obtained by plotting $\ln(\beta/T^2)$ against $1/T$ is interpreted as $-E_a/R$, and thus the activation energy for the relevant decomposition step can be calculated.

$$ln\frac{\beta}{T^2} = ln\frac{A.R}{E_a.g(\alpha)} - \frac{E_a}{R.T} \quad (1)$$

The Flynn–Wall–Ozawa (FWO) method allows the calculation of the apparent activation energy using data obtained from different heating rates at a given degree of transformation, without requiring any assumptions about the reaction mechanism. In its mathematical form, the inverse of the natural logarithm of the heating rate and the corresponding transformation temperature forms a linear relationship. According to the FWO Eq. (2), β is the heating rate, T is the maximum decomposition temperature, A is the pre-exponential factor, R is the gas constant and E_a is the activation energy, α is maximum conversion rate and the slope of the linear equation in logarithmic form obtained from the $1/T$ plot against lnb is equal to $-1.052\ E_a/R$ and from here the activation energy can be calculated. Thus, the activation energy can be directly calculated using the slope. In this respect, the FWO method is a powerful and mechanism-independent kinetic analysis technique that allows the activation energy to be determined separately for each degree of transformation, even in systems exhibiting multistep decomposition [35,36].

$$ln\beta = ln\frac{A.E_a}{R.G(\alpha)} - 5.331 - 1.052\frac{E_a}{R.T} \quad (2)$$

Fig. 3a shows the TG/d[TG] thermograms of the P9 sample at different heating rates. To determine the kinetic parameters of a three-step degradation mechanism of the activated carbon sample, graphs drawn by applying the data obtained from the TG analysis at different heating rates to the KAS and FWO equations are given in Fig. 3, respectively. The calculated activation energies and regression coefficient values are given in Table 2. The regression coefficient values obtained by applying the experimental data to the KAS and FWO models are quite close to each other. The regression values for the thermal degradation stages given in the table are calculated as 0.8026, 0.9140, and 0.9980 for the KAS equation, and 0.7499, 0.9200, and 0.9996 for the FWO equation, respectively. The activation energies in these decomposition steps were calculated as 31 kJ/mol, 32 kJ/mol, 205 kJ/mol according to the KAS method and 36 kJ/mol, 39 kJ/mol, 221 kJ/mol according to the FWO method, respectively. Based on thermal analysis diagrams at different heating rates, the first degradation stage, where moisture and volatile components are removed, and the second degradation stage, where hemicellulose and cellulose are decomposed, show that the pyrolysis rate is slower than the third degradation stage, which is attributed to the degradation of lignin and the physical and chemical transformations of activated carbon. In other words, pyrolysis occurs more slowly at lower temperatures [37,38]. Thermal kinetic analysis of activated carbons reported in the literature reveals complex decomposition mechanisms, with activation energies determined by advanced thermogravimetric analysis techniques typically ranging from 95 to 177 kJ/mol. Song et al. (2013) used *iso*-transformation methods to obtain kinetic parameters and found activation energies of approximately 96.59 kJ/mol [39]. Liu et al. (2012) showed differences in activation energy calculations depending on the analysis method, ranging from 95 to 178 kJ/mol [40]. Mahani et al. (2011) found an activation energy of 172.25 kJ/mol for activated carbon obtained from peanut shells [37]. These studies highlight the importance of precise measurement techniques, demonstrating that the heating rate changes the decomposition temperatures, the activation energy varies according to the material source and analysis method, and the complexity of thermal kinetic analysis in activated carbons.

3.1.3. SEM/EDX analysis

In this study, the SEM images of the surface morphologies of P0 and biochars (P1-P9) produced under different conditions were examined at 1.5 KX and 4 KX magnifications and given in Fig. 4. The SEM image of raw cotton waste (P0) given in Fig. 4 shows that the fibrous and natural cellulosic structure is preserved. The porosity of the raw sample is extremely limited in accordance with the literature [41,42]. The SEM images of P1 and P2 obtained by pyrolysis in an inert environment at 300 °C and 800 °C are given, respectively. The pyrolysis process carried out at low temperature caused a partial thermal decomposition in the biomass.

Table 2
Activation energy calculated from KAS and FWO methods for P9 sample.

Thermal degradation steps	Kinetic models			
	KAS		FWO	
	Ea (kj/mol)	R^2	Ea (kj/mol)	R^2
1	31	0.7499	36	0.8026
2	32	0.9200	39	0.9140
3	205	0.9996	221	0.9980

However, the development of the pore structure did not occur and the morphology exhibited a compact structure. This shows that low temperature is insufficient for carbonization and porosity. The high-temperature pyrolysis process caused more pronounced surface deformations compared to low-temperature pyrolysis, and a porous structure was observed to form, although in a very limited manner. However, applying only thermal treatment is not sufficient for high surface area and effective adsorption [43]. In the SEM image of P4 obtained by applying physical activation with CO_2 gas at 800 °C for 3 h, significant porosity development in the structure of the biomass and a more open surface morphology and distinct voids were observed. Physical activation supported pore formation, but the irregularity of the pores and clogged regions revealed that CO_2 was not as effective as chemical activation. In the literature, this situation was explained by the development of pore formation observed in the structure during physical activation with CO_2 due to the release of volatile compounds as a result of thermal decomposition of the biomass. In this process, CO_2 gas reacted with the carbon surface, causing the structure to be hollowed out and the pores to open. Especially in cellulose-rich biomasses, such as peanut shells, a porous structure is formed with the carbonization of cellulose during the activation process. This transformation leaves a porous carbon matrix behind by separating the cellulose from the structure, thus increasing the surface area and adsorption capacity of the activated carbon. It is stated that pores develop more in amorphous structures and surface layers rather than in tight regions between crystallites [44,45]. When the SEM images of P5 and P6 produced by applying chemical activation with KOH at impregnation ratios of 1:10 and 1:20, respectively, are examined in Fig. 4, striking differences are seen in terms of surface morphology. In the 1:10 sample, a dense porous structure was formed in the carbon skeleton due to the high KOH ratio per gram of biomass, and the surface was clearly fragmented and activated. In the 1:20 sample, porosity remained at a lower level due to the lower amount of KOH per gram of biomass. These results prove that the activation agent ratio has a direct effect on pore development. In the

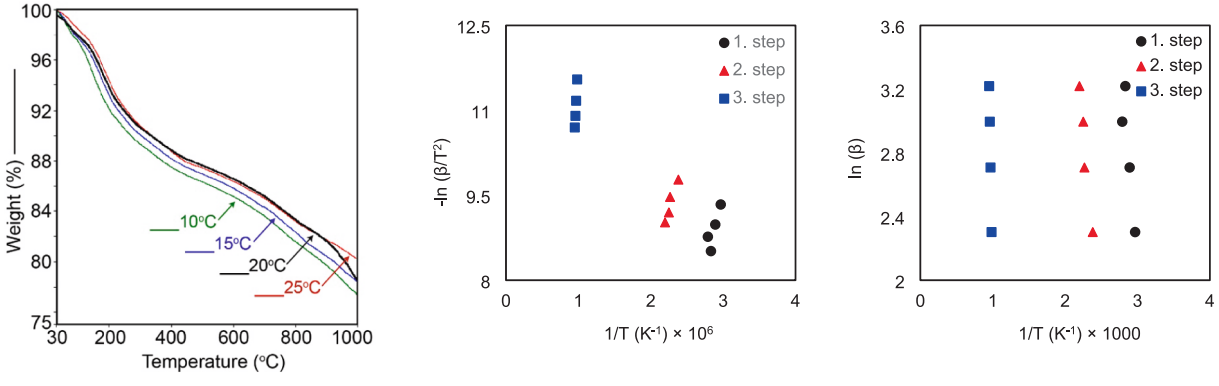

Fig. 3. A) tg/d[tg] curves of p9 at different heating rates, b) the plots of $-\ln(\beta/T^2)$ versus 1/T for KAS model and c) The plots of $\ln(\beta)$ versus 1/T for FWO model.

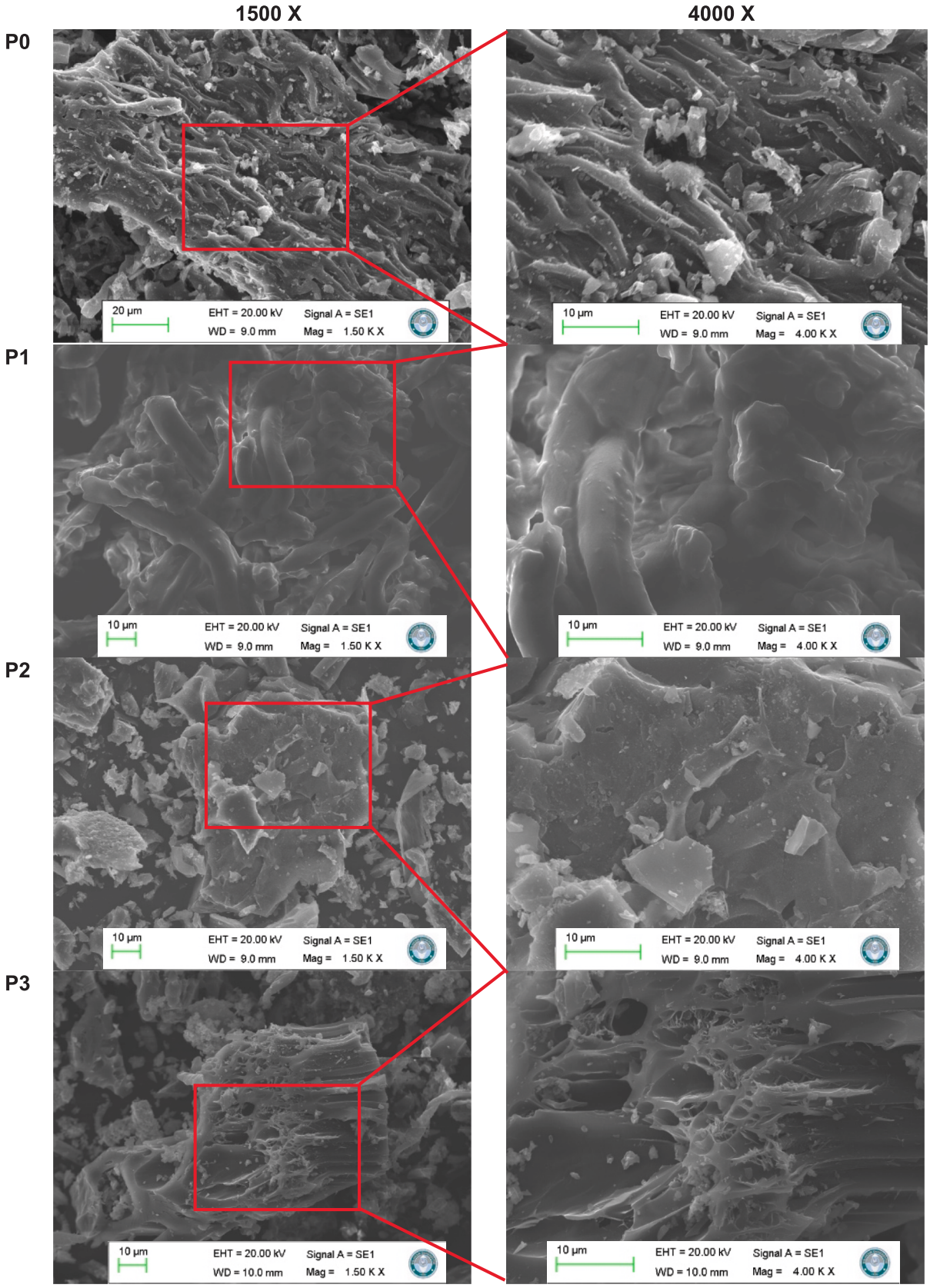

Fig. 4. SEM images of biomass and biochars.

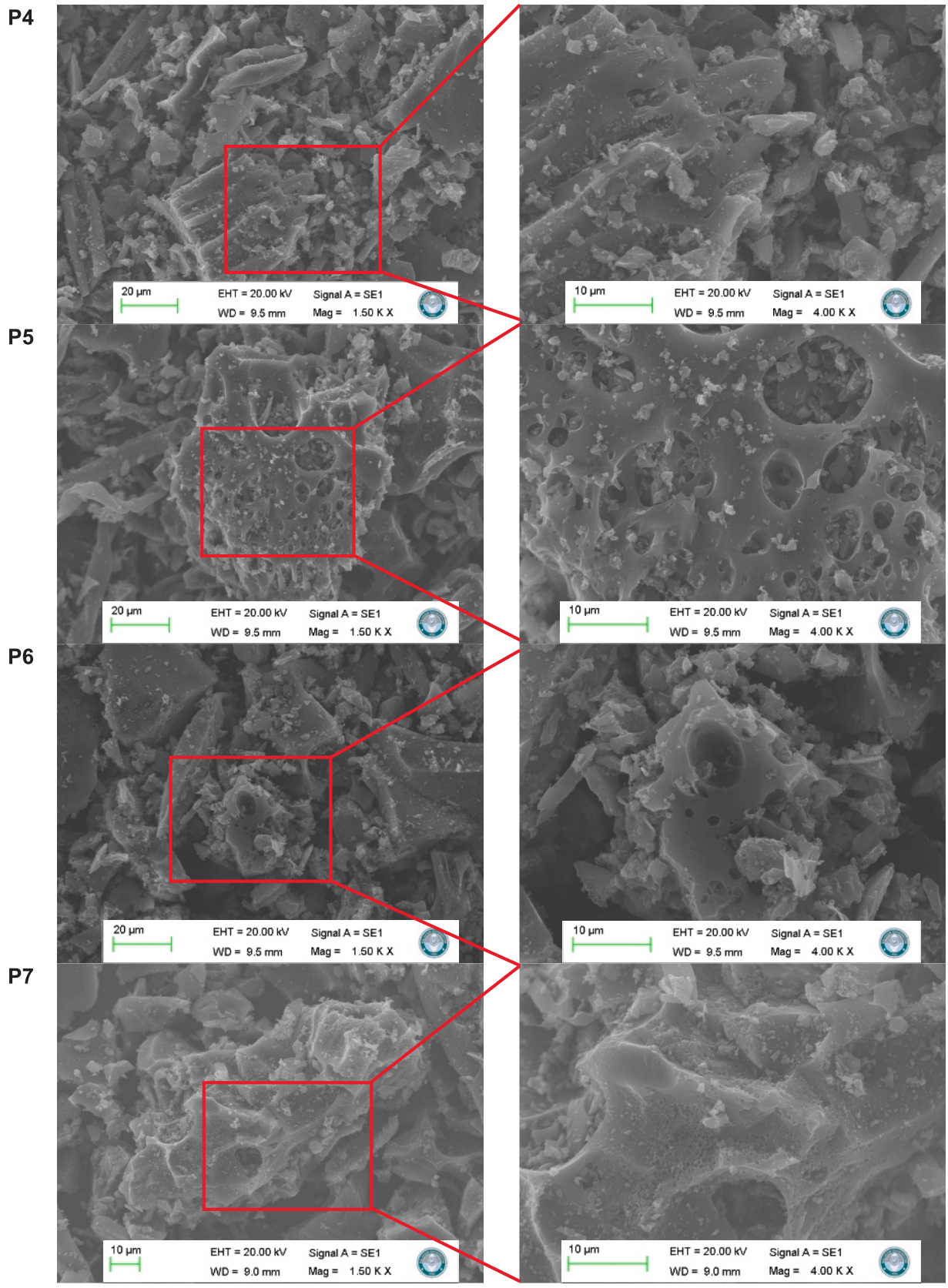

Fig. 4. (*continued*).

SEM image of P6, which was produced by using physical activation and chemical activation methods together, it is seen that there are pores, the pores are more homogeneously distributed and the carbon skeleton opens more regularly [46]. When the surface morphology of P7 is examined, it is understood that low CO_2 flow (25 mL/min) causes the activation to be limited and the pores develop less. In P8, porosity

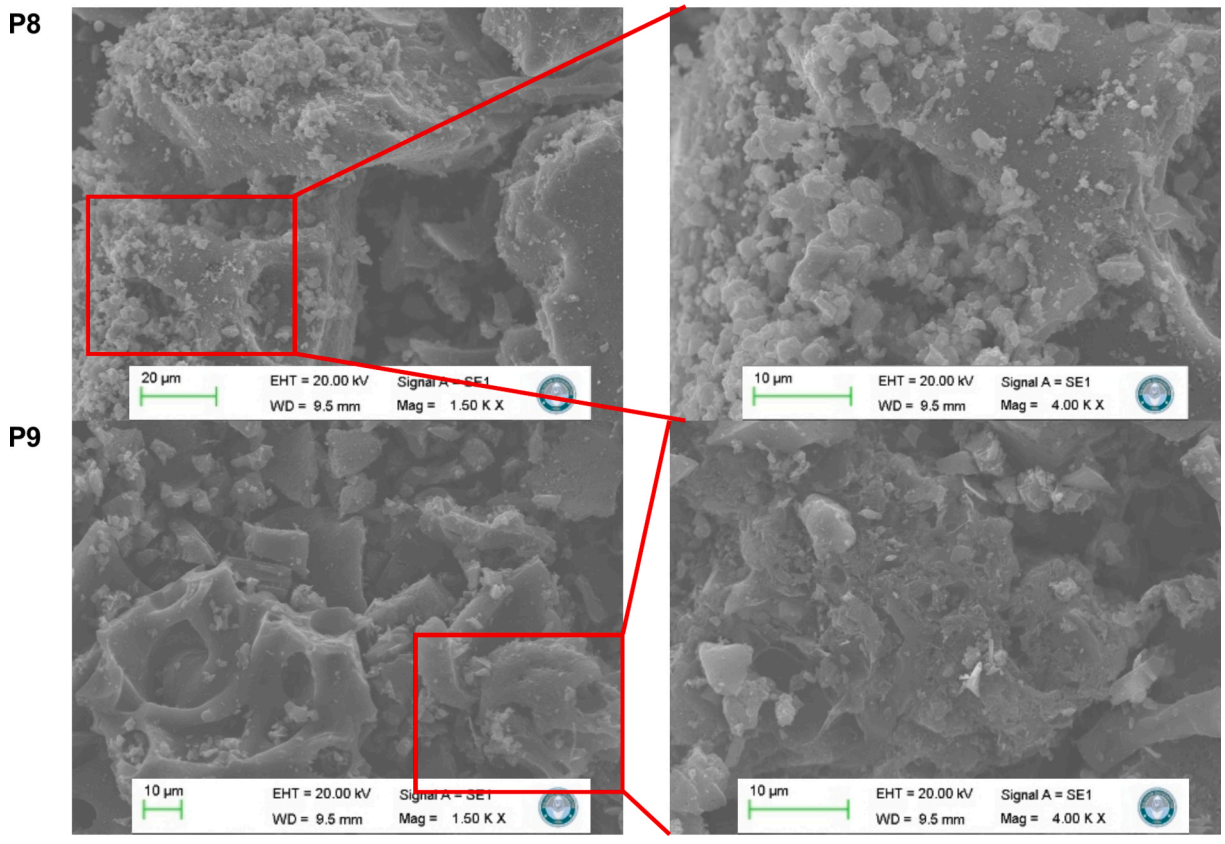

Fig. 4. (*continued*).

increased with medium gas flow (50 mL/min) and the surface gained a more open morphology. In P9, high gas flow (100 mL/min) caused more carving of the carbon structure and a wide and dense pore network was formed. These results show that the gas flow rate is a determining parameter on the physical activation efficiency. SEM images show that synthesis parameters have significant effects on biochar structure. Chemical activation provides high porosity, especially with the use of KOH, while physical activation offers a more environmentally friendly but relatively limited pore structure. Using physical and chemical activation methods together provides a more balanced and functional carbon structure by combining the advantages of both methods.

The elemental compositions of biochars obtained with different activation methods were determined by Energy Dispersive X-Ray Spectroscopy (EDX) analysis (see Table 3). In the elemental analysis of P0, 60.52 % carbon, 34.84 % oxygen and trace amounts of potassium, copper, phosphorus, magnesium, sulfur, calcium and chlorine were determined. The high oxygen content of P0 can be attributed to the oxygenated functional groups belonging to the characteristic composition of structural polymers such as cellulose, hemicellulose and lignin in its structure [47,48]. While the carbon content of P1 increased to 74.38 %, the oxygen content decreased to 22.06 %. This shows that the volatile compounds were partially removed by the limited pyrolysis process at low temperature and the structure became more carbon-heavy. Nevertheless, the presence of high oxygen levels indicates that the functional groups in the structure are significantly protected by pyrolysis at 300 °C. In P2 produced by pyrolysis at 800 °C, 69.63 % carbon and 12.72 % oxygen content were detected, indicating that the sample underwent advanced carbonization. In this sample, it was observed that elements such as potassium (3.26 %), calcium (2.71 %), chlorine (4.16 %), magnesium, phosphorus and fluorine increased significantly. This can be explained by the concentration of inorganic structures in the biomass during pyrolysis and their accumulation as residue on the surface. In P3, the carbon level was measured as 71.73 % and the oxygen level as 15.52 %. This shows that the physical activation performed with CO_2 protects the oxygenated surface groups to some extent. The most striking element is the presence of Cu (copper) at 11.87

Table 3
Elemental amounts of biomass and biochars determined by EDX.

Samples	Elements (wt.%)														
	C	O	K	Cu	P	Mg	S	Ca	Cl	Fe	Si	P	Na	Al	Zn
P0	60.52	34.84	1.42	1.05	0.74	0.54	0.38	0.28	0.23	–	–	–	–	–	–
P1	74.38	22.06	1.43	0.47	0.81	0.54	–	0.32	–	–	–	–	–	–	–
P2	69.63	12.72	3.26	–	0.99	1.44	0.63	2.71	4.16	0.34	0.23	0.99	0.35	0.11	2.12
P3	71.73	15.52	0.16	11.87	–	0.02	–	0.12	0.36	–	0.18	–	–	0.03	–
P4	83.42	11.28	0.23	1.81	–	0.21	0.68	0.42	1.05	0.57	0.20	–	0.12	–	–
P5	79.75	12.91	0.81	1.68	–	0.71	0.43	0.42	1.48	0.35	1.41	–	–	0.04	–
P6	84.14	9.04	1.07	1.41	–	0.23	0.60	0.20	2.07	–	0.18	0.96	0.13	–	–
P7	89.11	7.90	0.24	–	–	0.17	0.78	–	1.01	0.58	–	–	–	–	–
P8	88.92	9.46	–	–	–	–	0.32	–	0.17	1.14	–	–	–	–	–
P9	85.30	12.07	–	–	–	–	0.48	0.11	0.04	1.87	0.13	–	–	–	–

%. The elevated Cu signal observed in sample P3 originates from the SEM sample holder and coating material rather than from the activation process. This was confirmed as an isolated instrumentation-related artifact. Importantly, sample P3 was not included in hydrogen storage measurements, and therefore, this contamination does not affect any adsorption results. P4 (1:10 KOH ratio) and P5 (1:20 KOH ratio) samples produced by KOH chemical activation clearly reflect the effects of chemical activation. The carbon ratios are 83.42 % and 79.75 %, respectively, and the oxygen ratios are 11.28 % and 12.91 %, respectively, and a purer carbon structure is obtained in sample P4 with high KOH ratio. Some inorganic elements such as K, Cl, Ca and F were detected in both samples. Activation with KOH made the carbon skeleton more active by removing oxygenated surface groups [49]. P6 contains 84.14 % carbon and 9.04 % oxygen. The combination of chemical activation with KOH and physical activation with CO_2 provided a large removal of oxygenated groups in the carbon structure. The fact that elements such as K, Cl and Na can still be detected shows that the washing process after activation did not completely remove trace elements. This combined method, which was applied by subjecting samples chemically activated with KOH to physical activation at different CO_2 flow rates, led to more advanced carbonation in the biomass and this change was also reflected in the elemental

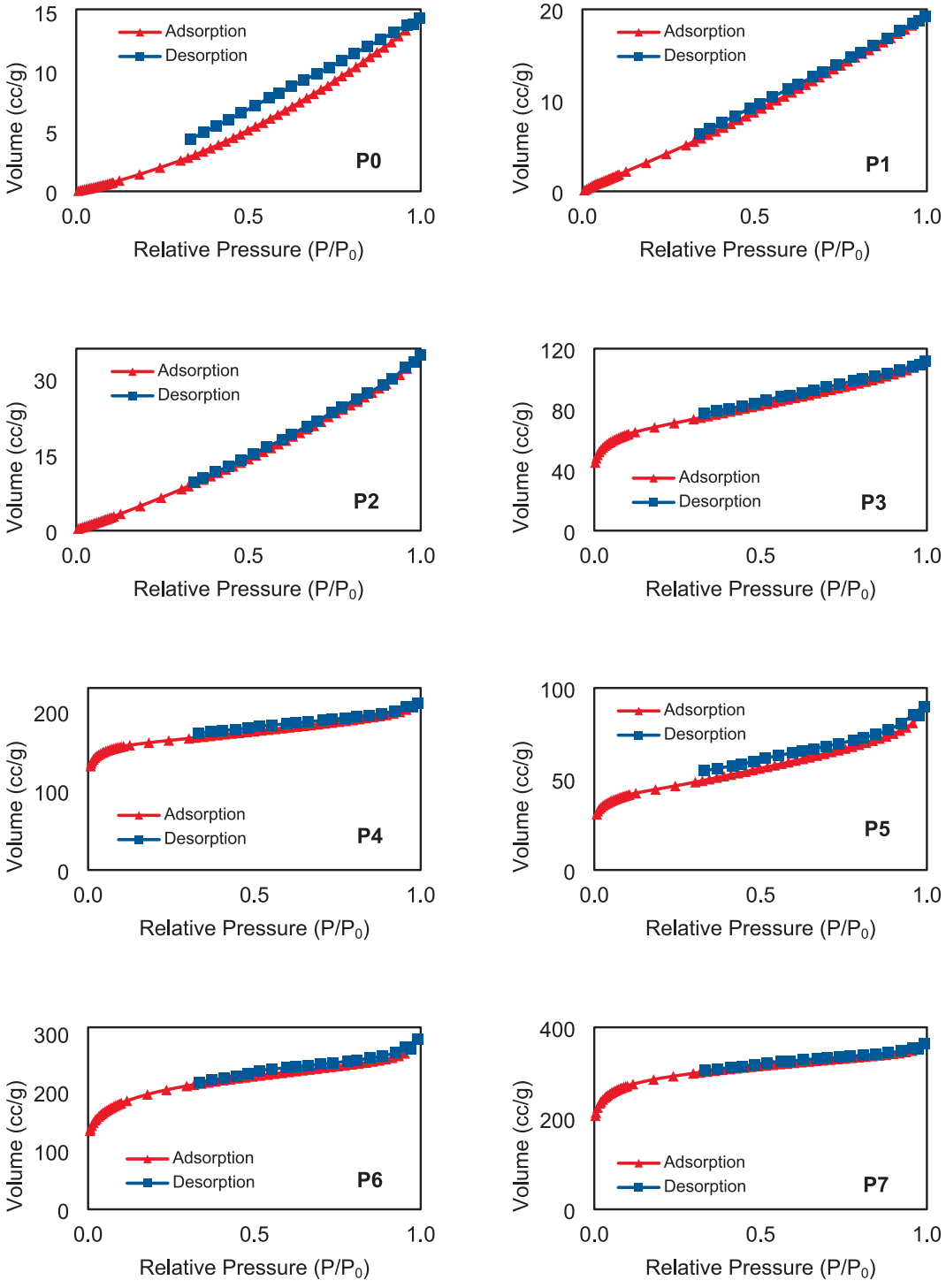

Fig. 5. N_2 adsorption–desorption isotherm plots of P0-P9 samples.

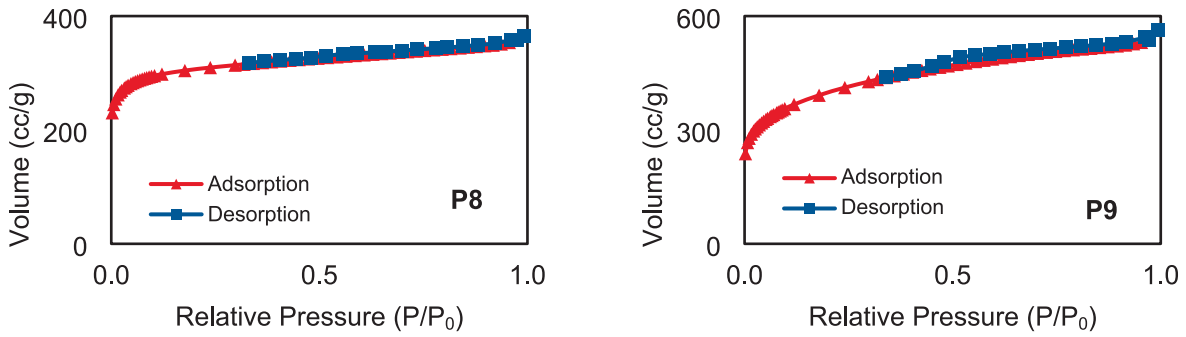

Fig. 5. (*continued*).

compositions: P7 obtained with 25 mL/min CO_2 has the highest carbon content with 89.11 % carbon and 7.90 % oxygen. This situation can be associated with a well-developed porous structure and low surface oxidation. P8 obtained with 50 mL/min CO_2 has a carbon content of 88.92 % and oxygen of 9.46 %. P9 obtained with 100 mL/min CO_2 has a carbon content of 85.30 % and oxygen of 12.07 %. The increase in oxygen ratio may indicate that high CO_2 flow rate in presence of KOH leads to the re-formation of some oxygenated functional groups in the structure.

3.2. Hydrogen storage

In this study, porous biochars were produced from cotton waste under different pyrolysis conditions. Nitrogen adsorption–desorption isotherm plots of biochars produced by pyrolysis method under inert nitrogen atmosphere at different temperatures are given in Fig. 5. When the nitrogen adsorption–desorption isotherms of P0–P9 are evaluated according to the IUPAC classification, it is observed that P0–P3 exhibit Type II isotherms, indicating structures with low specific surface areas and limited pore volumes. P4–P7, on the other hand, display a steep increase in adsorption at low relative pressures followed by a plateau, consistent with Type I isotherms, suggesting the presence of predominantly wider microporous structures. The sharp adsorption uptake at very low relative pressures ($P/P_0 < 0.1$) in these Type I profiles indicates that hydrogen is stored primarily through a micropore filling mechanism rather than layer-by-layer surface adsorption, which is characteristic of narrow micropores (<2 nm) and directly supports the role of microporosity in hydrogen storage. In P8 and P9, the appearance of Type IV isotherms accompanied by pronounced hysteresis loops reveals the coexistence of microporosity and mesoporosity, with capillary condensation mechanisms playing a significant role. Among them, sample P9 stands out with the highest adsorption capacity and a broad hysteresis loop, reflecting the highest BET surface area and pore volume. The presence of hysteresis is indicative of pore network effects, possibly due to constrictions or pore blocking phenomena. In conclusion, the isotherm types and hysteresis behaviors provide valuable insights into the micro- and mesoporous characteristics of the samples, and P9 appears to be the most promising candidate for adsorption-based applications due to its high surface area and well-developed pore structure [50]. Again, the relationships between cumulative pore volume and pore diameter of P0 and biochar samples are presented in Fig. 6. According to the generally accepted classification, pores with diameters smaller than 2 nm are defined as microporous, pores in the range of 2–50 nm are defined as mesoporous, and those larger than 50 nm are defined as macroporous structures. In order to evaluate the pore structure more precisely, the derivatives of the relevant cumulative pore volume-pore diameter curves were taken to support the analyses (Fig. 6). In addition, BET surface area, total pore volume (V_t), micropore volume (V_{micro}), mesopore volume (V_{meso}), macropore volume (V_{macro}) and DFT (Density Functional Theory) based pore volume (V_{DFT}) values calculated based on the adsorption–desorption isotherm curves given in Fig. 5 and the cumulative pore volume-pore diameter curves in Fig. 6 are summarized in Table 4. The BET surface areas of biochars produced from cotton waste pyrolyzed at 300 °C (P1) and 800 °C (P2) were measured as 28 m^2/g and 49 m^2/g, respectively. This increase in temperature caused an increase of approximately 100 % in the surface area. This situation is explained by the fact that organic components decompose more at high temperatures and turn into gaseous and volatile products [51]. At low temperatures, lignocellulosic biomass is converted into more carbon-rich solid products; as the temperature increases, the volatile products and gas phase increase, and the amount of remaining solid residue decreases. In addition, high temperatures increase water loss and dehydration reactions, leaving less residue and facilitating the exit of residues such as tar and ash from the structure. This process ensures the effective removal of volatile substances in the carbon structure, and accordingly, the BET surface area increases, and a more developed pore structure is obtained [52]. When Table 4 is examined, a significant increase in total-, micro-, meso- and macropore volumes is observed with the increase in pyrolysis temperature. For example, the total-, micro-, meso- and macropore volumes of P1 pyrolyzed under nitrogen atmosphere at 300 °C are 0.030, 0.005, 0.022 and 0.003 cc/g, respectively, while the total-, micro-, meso- and macropore volumes of P2 pyrolyzed at 800 °C are 0.054, 0.018, 0.019 and 0.007 cc/g, respectively. This result was similarly observed in biochars obtained by the pyrolysis of woody biomass and is consistent with previous findings in the literature [52,53].

The effects of carbon dioxide (CO_2) and nitrogen (N_2) gases on the BET surface areas of biochars produced by pyrolysis at 800 °C show significant differences. While the BET surface area of biochar produced under nitrogen atmosphere is 49 m^2/g, the BET surface area of P3 produced under carbon dioxide atmosphere is 254 m^2/g. Again, the total-, micro-, meso- and macropore volumes of P2 produced under nitrogen atmosphere are 0.054, 0.018, 0.019 and 0.007 cc/g, while the total-, micro-, meso- and macropore volumes of P3 produced under carbon dioxide atmosphere are calculated as 0.173, 0.103, 0.051 and 0.019 cc/g, respectively. The increase in the BET surface area of biochar under carbon dioxide atmosphere is parallel to the increase in pore volume. The use of CO_2 atmosphere provides biochar with higher carbon and lower oxygen content, which is consistent with EDX analysis; this improves the surface structure of biochar while also creating more porosity. Under N_2 atmosphere, biochar generally results in a lower surface area. Therefore, CO_2 provides a more effective environment than N_2 in increasing the BET surface area and pore volume of biochar [54,55].

In the study, hydrogen storage capacities of porous biochars produced under different conditions were measured at room and cryogenic temperatures in a wide pressure range. Hydrogen storage capacities of samples vary depending on BET surface area and pore volume. Therefore, hydrogen storage capacities of P1, P2, P3 and P5 samples with low surface area and pore volume in Table 4 were not measured. Fig. 7 shows the pressure-dependent hydrogen storage capacities of P4, P6, P7, P8 and P9 samples at room and cryogenic temperatures. Biochar samples

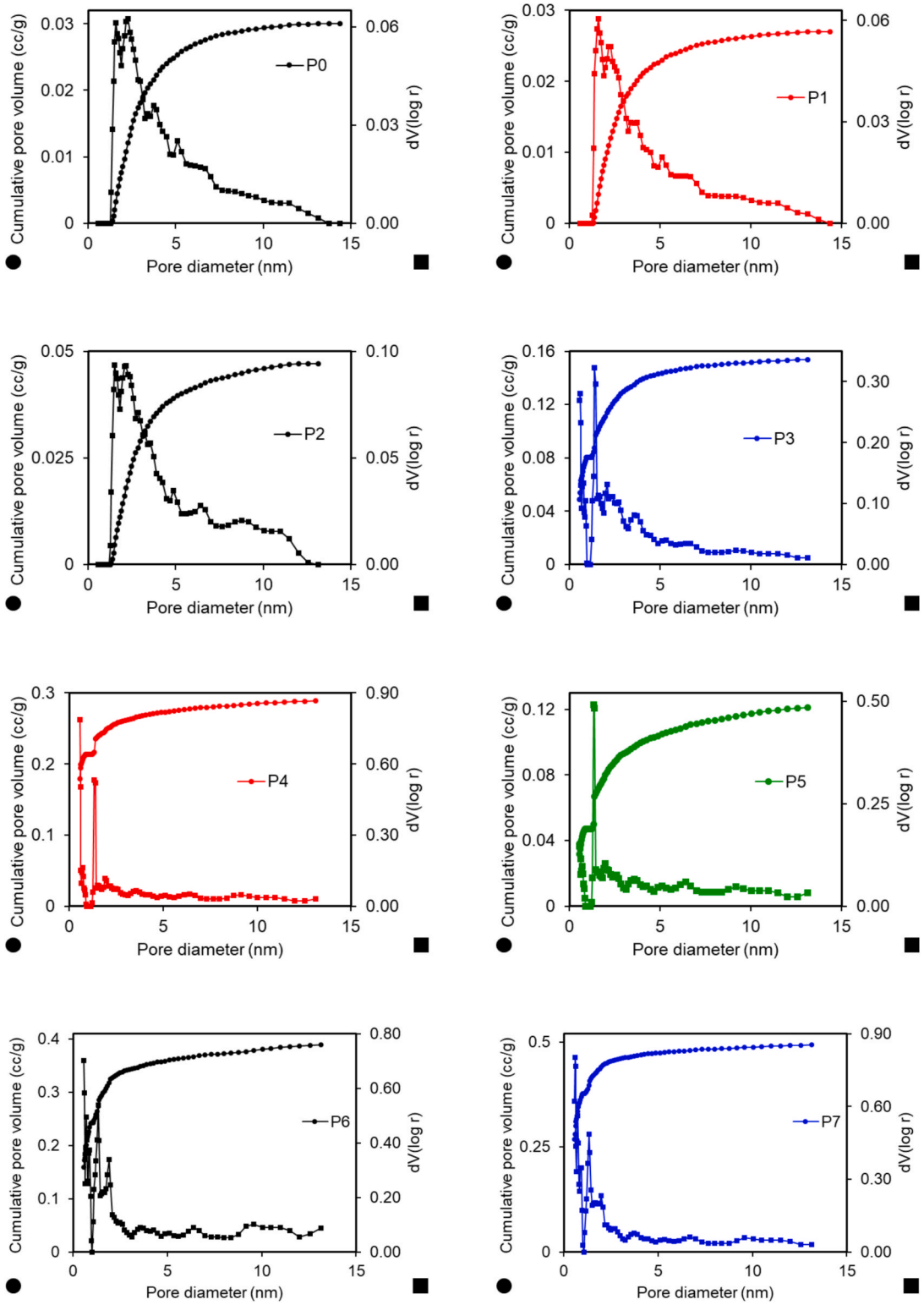

Fig. 6. The plots of cumulative pore volume versus pore diameter of biomass and biochars.

from the figures exhibit different behaviors at room and cryogenic temperatures. Hydrogen storage capacities of samples increase linearly with increasing pressure at room temperature. These results are in good agreement with Henry's law. As a result of increasing density of gas with increasing pressure, van der Waals attractive forces between gas molecules and between gas molecules and biochar samples increase. This causes an increase in hydrogen storage capacities of samples. At cryogenic temperature, the storage capacity increases rapidly with increasing pressure at the beginning, decreases without reaching a plateau and reaches a maximum when the pressure continues to increase, and the storage capacity increases again when the pressure is increased further. The maximum observed in the isotherm curve is due

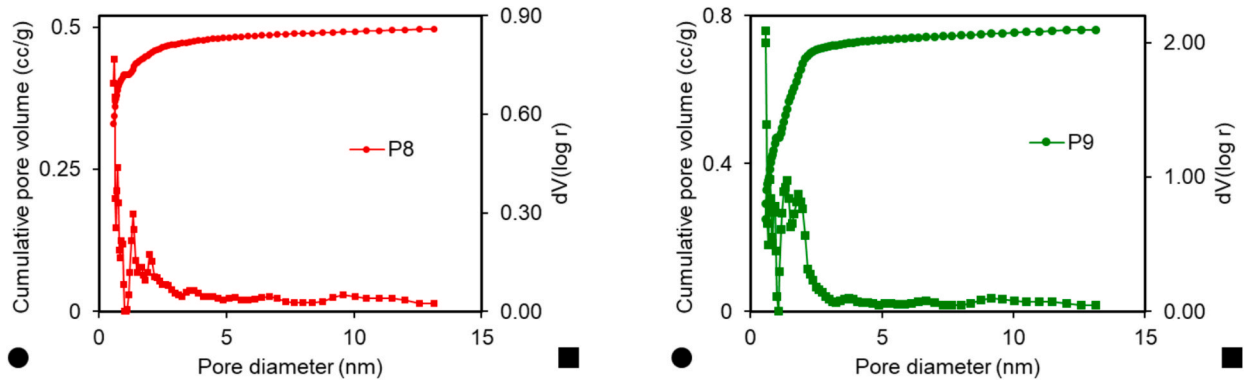

Fig. 6. (*continued*).

Table 4
BET surface areas and pore volumes of biomass and biochar samples.

Samples	S_{BET} (m^2/g)	V_t (cc/g)	V_{micro} (cc/g)	V_{meso} (cc/g)	V_{macro} (cc/g)	V_{DFT} (cc/g)
P0	25	0.022	0.002	0.018	0.002	0.020
P1	28	0.030	0.005	0.022	0.003	0.027
P2	49	0.054	0.018	0.019	0.007	0.047
P3	254	0.173	0.103	0.051	0.019	0.154
P4	628	0.327	0.252	0.037	0.038	0.289
P5	165	0.139	0.068	0.054	0.017	0.122
P6	724	0.448	0.294	0.096	0.058	0.390
P7	1085	0.564	0.436	0.059	0.069	0.495
P8	1188	0.564	0.471	0.028	0.065	0.499
P9	1446	0.873	0.570	0.197	0.106	0.767

to the excessive adsorption of hydrogen molecules. Excessive adsorption is an event that occurs after the amount of adsorption of a gas, molecules or liquid through physical and chemical interactions on an adsorbent surface at a certain temperature and pressure reaches the monolayer adsorption limit [56]. Generally, in experiments conducted at low pressures, the effect of interactions between the gas phase on the adsorbent and the adsorbent is more pronounced. In this case, as the density of the gas increases in the pores and on the surface of the adsorbent, it becomes possible to store more gas. A similar situation has been observed for activated carbons produced from horse chestnut in the pressure range of 20–30 bar. This situation occurs as a result of the hydrogen concentration that the activated carbons can adsorb reaching the highest point with the applied pressure; at this point, it is not possible to adsorb more hydrogen and it is also defined as the excessive adsorption isotherm not showing a smooth curve [57]. The mechanism usually occurs by the addition of adsorbate molecules to the existing molecules on the surface. However, at a certain point, when more pressure is applied, the density of the gas will increase. This means that the active points on the surface for gas molecules decrease and therefore the excessive adsorption capacity begins to decrease. Excessive adsorption is widely used to compare the adsorption properties of microporous materials in particular and shows a strong relationship with the surface area and pore volume of these materials [5]. As a result, the gas storage capacity decreases at high pressures because the molecules are pushed from the outside to the inside, resulting in the filling of the pores. As can be seen from the figures, excessive adsorption occurs in the pressure range of 12–17.5 bar in this study. A similar situation was observed in the range of 15–25 bar for activated carbons produced from tangerine peel by $ZnCl_2$ and KOH activation and subsequent carbonization processes [58]. Fig. 7a and b show the hydrogen storage capacities of biochars produced from cotton waste pyrolyzed under different conditions at room and cryogenic temperatures, respectively. It is seen from the figure that the sample with the highest hydrogen storage capacity is P9, followed by P8, P7, P6 and P4, respectively. Table 4 also

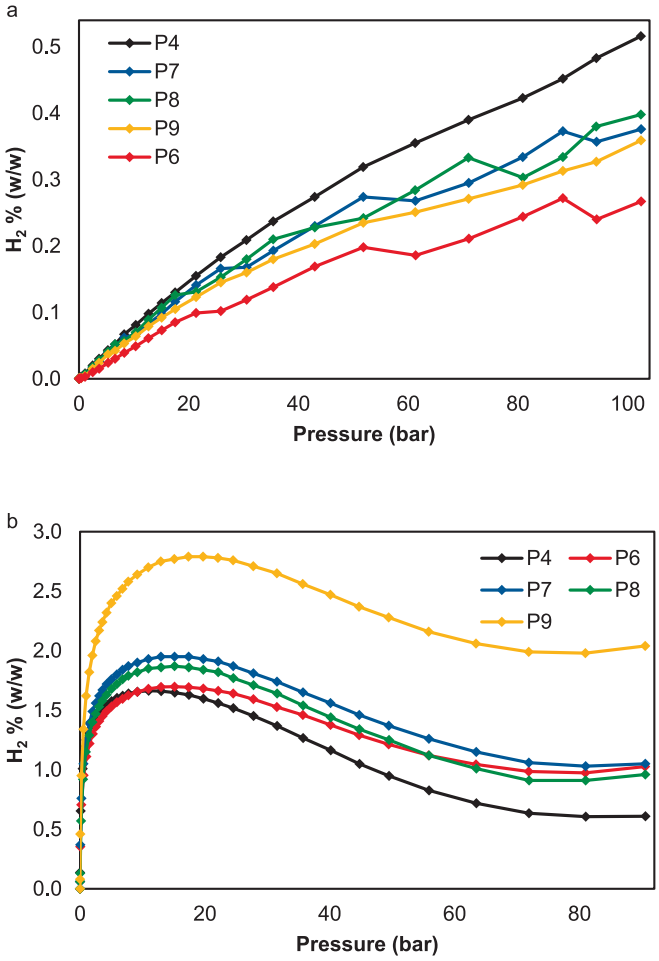

Fig. 7. Hydrogen storage capacities of P4, P6, P7, P8 and P9 samples at a) room and b) cryogenic temperatures.

shows the BET surface areas and pore distributions of biochars produced as a result of pyrolysis at 800 °C at different KOH/cotton waste ratios (1:10 (P4) and 1:20 (P5)) under nitrogen atmosphere. The data show that the BET surface area and pore volume decrease with the decrease in the KOH/biomass ratio. The BET surface area, and total-, micro-, meso- and macropore volumes of P4 produced at 1:10 KOH/cotton waste ratio are 628 m^2/g, and 0.327, 0.252, 0.037 and 0.038 cc/g, respectively, while the BET surface area, and total-, micro-, meso- and macropore volumes of P5 produced at 1:20 KOH/cotton waste ratio are 165 m^2/g, and 0.139, 0.068, 0.054 and 0.017 cc/g, respectively. Low KOH/

biomass ratios do not provide sufficient activation, resulting in low surface areas. However, high levels of KOH both act as a catalyst in the carbonization process, providing gasification of organic components in lignocellulosic biomass, and also help open new pores by increasing the interaction of potassium with carbon dioxide at high temperatures. This process leads to the creation of more surface area and, as a result, an increase in the BET surface area [59]. For this example, the amount of hydrogen stored at the pressure value (13 bar) where excessive adsorption occurs is 1.66 wt%. Chahine's rule states that the adsorbent will have a hydrogen storage capacity of approximately 1 wt% for every 500 m^2/g surface area at cryogenic temperatures [60]. This value is well above the Chahine rule.

The hydrogen storage capacity of P6 pyrolyzed under carbon dioxide atmosphere at a constant 1:20 KOH/biomass ratio at 800 °C is higher than that of P4. Both the BET surface area and pore volume of P6 are higher than that of P4. The BET surface area and total-, micro-, meso- and macropore volumes of P6 produced under CO_2 atmosphere at a constant KOH/biomass ratio (1:20) at 800 °C were analyzed as 724 m^2/g, and 0.448, 0.294, 0.096 and 0.058 cc/g, respectively. Micropore volume is a highly determining factor in the adsorption of hydrogen in solid adsorbents [5]. As can be seen from Table 4, the micropore volume of P6 is higher than that of P4. In this section, it is necessary to evaluate the effects of both pyrolysis atmosphere and KOH together. Pyrolysis atmosphere significantly affects the properties and reactivity of biochar. CO_2 atmosphere generally increases biochar reactivity compared to N_2. The reason why biochar produced under CO_2 atmosphere has a higher BET surface area than N_2 atmosphere is that CO_2 acts as an active medium and promotes gasification during pyrolysis. This process allows more effective removal of volatilities and more fragmentation of the biomass structure, creating more open pore space. In addition, CO_2 environment increases the surface area and causes more active surface area to be formed due to the more devolatilization of carbon in the biochar structure [61]. In addition, the presence of KOH contributes to the formation of pores in the carbon matrix and thus to the increase in surface area. Therefore, it can be said that the P6 has a higher storage capacity than P4 due to the adsorption of hydrogen molecules in the active points on its surface and micropores. The hydrogen storage capacity of P6 at excessive adsorption pressure (15.14 bar) was determined as 1.70 wt%. This value is slightly higher than that of P4.

Fig. 7 also shows the hydrogen storage capacities of P7, P8 and P9 produced by pyrolysis method at 800 °C and 1:10 KOH/biomass ratio and different CO_2 flow rates. The amount and type of gas present in the pyrolysis medium affect the BET surface area and pore volume of the produced porous biochar. It is observed that the BET surface areas and pore volumes of biochars produced under CO_2 atmosphere at constant pyrolysis temperature (800 °C) and KOH/biomass ratio and different flow rates increase with increasing CO_2 flow rate. BET surface areas of biochars produced at 25, 50 and 100 mL CO_2 flow rates per minute are 1085, 1188 and 1446 m^2/g, respectively. Similarly, total-, micro-, meso- and macropore volumes of biochars produced at 25, 50 and 100 mL CO_2 flow rates per minute were calculated as 0.564, 0.436, 0.059 and 0.069 cc/g; 0.564, 0.471, 0.028, 0.065 cc/g; and 0.873, 0.570, 0.197 and 0.106 cc/g, respectively. The results show that with the increase of CO_2 flow rate, the BET surface area of biochar increases and it becomes more microporous. This is because CO_2 atmosphere promotes gasification of carbon by increasing the porosity in the internal structure of biochar at high temperatures, which leads to the formation of more micropores. In addition, CO_2 acts as a strong activator, which helps in further decomposition of residues in biochar and thus increases the surface area. As a result, the presence of CO_2 changes the structural properties of biochar and provides higher surface areas [62,63]. It is observed that the hydrogen storage capacities of P7, P8 and P9 increase in parallel with the increase in BET and pore volumes. It can be said that the storage capacity of P9 is quite high compared to other samples. The storage capacities of P7, P8 and P9 at excessive adsorption pressures (15.14, 12.96 and 17.36 bar) are 1.86, 1.95 and 2.79 wt%, respectively.

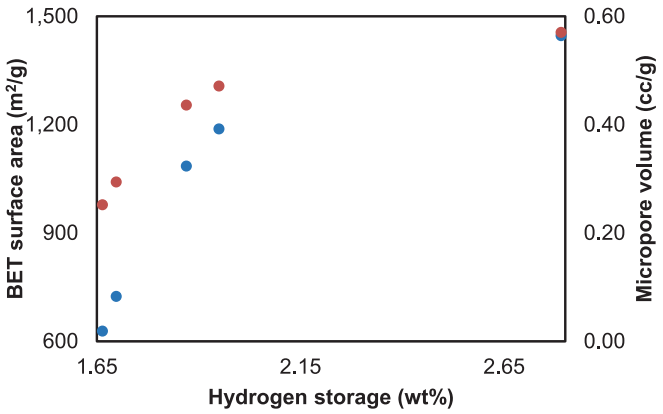

Fig. 8. The changing of hydrogen storage amounts of samples with BET surface area and micropore volume.

Fig. 8 shows the relationship between hydrogen storage capacity and both BET surface area and micropore volume for the five samples. Pearson correlation analysis indicates that there is a strong positive correlation between hydrogen storage capacity and both textural parameters, with correlation coefficients of 0.87 for BET surface area and 0.86 for micropore volume. This implies that hydrogen adsorption occurs predominantly through physisorption on high surface area domains and is further enhanced by the volumetric confinement provided by micropores. Linear regression analysis supports these findings, where a 1 wt% increase in hydrogen storage corresponds to approximately 638 m^2/g increase in BET surface area and 0.247 cm^3/g increase in micropore volume. The p-values obtained for the two regression models ($p = 0.055$ and $p = 0.062$) are close to the conventional statistical significance threshold ($p < 0.05$), which is attributed to the limited number of samples ($n = 5$). However, the pronounced linear trends observed across the dataset and the high correlation coefficients clearly support the presence of a physically meaningful relationship between hydrogen storage capacity and pore structure. In addition, the slope for the H_2 (wt%)–BET regression (0.0012) lies within a 95 % confidence interval of − 0.0000 to 0.0024, and the slope for the H_2 (wt%)–Vmic regression (2.9939) lies within a 95 % confidence interval of − 0.27 to 6.26, indicating wider uncertainty ranges due to sample size while still maintaining consistent directional behavior. Notably, sample P9, which exhibits the highest hydrogen storage capacity (2.79 wt%), also possesses the highest surface area and micropore volume, further reinforcing the structural contribution to adsorption. These findings collectively emphasize that micropore accessibility and pore-network efficiency are more decisive factors than solely maximizing total surface area in the design of high-performance hydrogen storage carbons.

Table 5 presents the hydrogen storage capacities of various carbon-based materials measured at 77 K under different pressure conditions, demonstrating the significant effects of both pressure and carbon structure on adsorption performance. For instance, porous carbons have been reported to store 2.4 wt% and 2.19 wt% hydrogen at 1 bar [64,65], while a markedly higher capacity of 4.0 wt% was achieved at 40 bar [10], indicating that increasing pressure considerably enhances hydrogen uptake in these materials. Activated carbons also exhibit a wide range of performance characteristics: Doğan et al. reported hydrogen storage capacities in the range of 0.96–1.67 wt% at 30 bar [58], whereas Işınkaralar et al. measured 1.94 wt% at 45 bar [7], and Sun and Webley recorded 2.00 wt% at 50 bar [66]. Furthermore, Türkyılmaz et al. reported a high capacity of 4.46 wt% at 30 bar [57], while Lionetti et al. observed 3.66 wt% at 70 bar [67]. Additional studies on activated carbons yielded capacities such as 2.55 wt% [56] and 2.1 wt% [68] at 30 bar, illustrating that hydrogen storage performance of activated carbons depends strongly on activation conditions and applied pressure. In comparison, carbon spheres displayed a lower capacity of

Table 5
Hydrogen storage capacities of some carbon-based materials.

Samples	Temperature (K)	Pressures (bar)	Hydrogen storage, wt%	References
Porous carbon	77	40	4	[10]
Porous carbon	77	1	2.4	[64]
Porous carbon	77	1	2.19	[65]
Activated carbon	77	30	0.96–1.67	[58]
Activated carbon	77	45	1.94	[7]
Activated carbon	77	30	4.46	[57]
Activated carbon	77	50	2.00	[66]
Activated carbon	77	30	2.55	[56]
Activated carbon	77	30	2.1	[68]
Activated carbon	77	70	3.66	[67]
Carbon sphere	77	30	1.1	[69]
Biochar	77	17.4	2.79	In this study

1.1 wt% at 30 bar [69], highlighting the role of material morphology and pore accessibility. The cotton-waste-derived biochar developed in this study stored 2.79 wt% hydrogen at 17.4 bar, placing it within the performance range of both porous carbons and activated carbons measured under similar cryogenic conditions. This result confirms that the activation strategy applied here effectively produces a carbon structure capable of competing with widely reported hydrogen storage materials.

3.3. Adsorption isotherms

Adsorption isotherm is the curve that shows how the amount of gas or liquid adsorbed on a solid surface changes depending on the pressure (or concentration) at constant temperature. These isotherms are used to understand the mechanism of adsorption and surface properties. They provide important information such as the porosity, surface area and adsorption capacity of the material. Therefore, it plays a critical role especially in catalyst, gas storage and environmental engineering applications [8,70].The most widely used isotherm models in the literature to explain the adsorption properties of gases are Freundlich, Langmuir, dual Langmuir and Temkin isotherms [70].

$$q_e = K_F P^{1/n} \tag{3}$$

Freundlich isotherm is an empirical model that describes multilayer adsorption occurring on heterogeneous surfaces. This model assumes that the adsorption energy varies across the surface and that each adsorption point may have different energy. The Freundlich isotherm works particularly well in low concentration ranges. The mathematical expression of the isotherm is:

$$lnq_e = lnK_F + 1/nlnP \tag{4}$$

Thanks to this linear expression, K_F and n values can be calculated from the plot of lnq_e against lnP [70].

The Langmuir isotherm is based on the assumption that monolayer adsorption occurs, the surface is homogeneous and the adsorption points are equi-energetic. In this model, only one molecule can bind to each surface point and there is no interaction between the adsorbed molecules. The Langmuir isotherm shows that the adsorption is fixed, especially when the saturation level is reached. The basic equation of the isotherm is:

$$q_e = \frac{q_{m1} K_1 P}{1 + K_1 P} \tag{5}$$

Where q_e is the adsorbed amount (mmol/g); P is the pressure (bar); q_{m1} is the maximum adsorption capacity (mmol/g); and K_1 is the Langmuir constant. The linear form of the equation is as follows:

$$\frac{P}{q_e} = \frac{1}{q_{m1} K_1} + \frac{P}{q_{m1}} \tag{6}$$

When the graph of P/q_e versus P is plotted in the linear equation, the slope of the line is $1/q_{m1}$ and the point where it intersects the y-axis is $1/q_{m1}K_1$, from which q_{m1} and K_1 can be calculated [70].

The dual-Langmuir isotherm is a model that assumes that there are two adsorption sites on the adsorbent surface with different energies. This model contains two separate Langmuir components representing both the high and low energy regions of the surface. The isotherm equation is as follows:

$$\frac{P^{1/2}}{q_e} = \frac{1}{K_2 q_{m2}} + \frac{P^{1/2}}{q_{m2}} \tag{7}$$

Where q_{m2} is the maximum adsorption capacity (mmol/g) and K_2 is the Langmuir constant [70].

Temkin isotherm is a model that takes into account the interactions between adsorbent and adsorbing molecules during adsorption, assuming that the adsorption energy decreases with the amount of surface coverage. According to this model, the heats of adsorption decrease logarithmically at high concentrations. Temkin isotherm gives good results especially in medium concentration ranges. The basic equation of the isotherm is:

$$q_e = AlnP + B \tag{8}$$

where q_e is the amount of adsorbed substance (mmol/g); P is the pressure (bar); A and B are constants related to the Temkin isotherm. Thanks to this linear equation, A and B values can be determined from the point where the slope and y-axis intersect [8].

The regression coefficients and related isotherm parameters calculated by applying the experimental data to the above isotherm equations are given in Table 6. In order to evaluate the fit between the experimental data and the isotherm models, the regression coefficient (R^2) values were taken into consideration. The R^2 value approaching 1 indicates that the model has a high accuracy in representing the experimental data. In this direction, the Langmuir isotherm model attracted attention with its very high R^2 values (0.9965–0.9982) in all samples and became the model providing the best fit with the experimental data. While the Langmuir model provided the highest fit with $R^2 = 0.9982$ in P4, the Dual-Langmuir model closely follows this model with $R^2 = 0.9919$. Similarly, the Langmuir isotherm stands out with R^2 values of 0.9978, 0.9980 and 0.9982 in P6, P7 and P8, respectively. Especially in P8, the low R^2 value (0.8395) of the Dual-Langmuir model indicates that this model is not suitable for the sample. In P9, the Langmuir model provides the best fit with $R^2 = 0.9965$. Although the Dual-Langmuir model exhibits high R^2 values in some samples, it shows less consistency compared to the Langmuir model when evaluated on a sample basis. Although the Freundlich isotherm model describes heterogeneous surface adsorption, it generally falls behind the Langmuir model with lower R^2 values (0.9335–0.9510). The Temkin model exhibited a moderate fit with R^2 values ranging from 0.9544 to 0.9843. These results indicate that adsorption mostly occurs in a monolayer and homogeneous manner on biochar surfaces. The high regression coefficients for the Langmuir isotherm model support that adsorption occurs in constant energy and equivalent surface regions. Although the relatively high R^2 values shown by the dual-Langmuir model in some samples indicate that there may be regions with different energy levels on the surface, this

Table 6
Isotherm analysis data for biochar samples.

Samples	Langmuir				Dual Langmuir	Freundlich			Temkin
	$q_{e(exp)}$ (mmol/g)	q_m (mmol/g)	K_1	R^2	R^2	n	K_F	R^2	R^2
P4	0.72	0.73	3.48	0.9982	0.9919	3.20	0.43	0.9439	0.9843
P6	0.76	0.78	1.94	0.9978	0.9903	3.10	0.41	0.9510	0.9586
P7	0.82	0.84	1.86	0.9980	0.9944	2.87	0.42	0.9482	0.9544
P8	0.77	0.79	1.72	0.9982	0.8395	2.42	0.35	0.9335	0.9816
P9	0.89	0.91	1.42	0.9965	0.9388	2.58	0.42	0.9364	0.9647

situation is not generalizable for all samples. In evaluating the compatibility of experimental data with the Langmuir isotherm, not only the R^2 value but also the closeness of the experimental adsorption capacity (q_e) and the monolayer capacity (q_m) values calculated from the Langmuir isotherm is an important indicator. When the data in the table are examined, it is observed that there are very small differences between the q_e and q_m values for all biochar samples. The error values for all samples are below 3 %, which is quite low and shows that the model highly overlaps with the experimental results. In addition, the low error ratios show that the model successfully predicts the adsorption capacity in the experimental system. The generally low error ratios show that the Langmuir isotherm model is successful not only in terms of theoretical fit but also in terms of practical accuracy. These data reinforce the assumption that adsorption occurs on a monolayer structure and that the surface has homogeneous active sites. As a result, both high R^2 values and the agreement between experimental and theoretical adsorption capacities clearly show that the Langmuir isotherm model is the most suitable model for biochar samples. In the literature, hydrogen and carbon dioxide adsorption experiments carried out on various adsorbents have been evaluated with different isotherm models. In high-pressure (up to 30 atm) studies for pure hydrogen and CO_2, it was observed that the Freundlich isotherm showed high agreement with the data. This model provided an effective description especially at low concentrations by considering the heterogeneous surface properties and multiple adsorption energy levels [71]. The analyses carried out on MOF-177 revealed that the hydrogen adsorption capacity was high due to the large pore volume and high specific surface area, and the Freundlich model successfully described this system [72]. Natural and acidic modified clinoptilolite samples also exhibited a strong correlation with the Freundlich model due to surface heterogeneity and multilayer structures [73]. In contrast, the Langmuir model for the adsorption of hydrogen on microporous adsorbents showed limited agreement at low temperature conditions because this model assumes surface homogeneity and single-layer adsorption, neglecting interactions between adsorbates. On the other hand, at low temperature and high pressure conditions, the Ono-Kondo model gave more accurate results with its structure including multilayer and interactions between adsorbates in microporous adsorbents (e.g. AX-21) [60]. Type I isotherm behavior was observed on functionalized nanoporous activated carbons and the effect of microporous structures was emphasized with the rapid saturation characteristic at low pressures. This showed a strong agreement with the experimental data, especially at 77 K. The low hysteresis behavior is also consistent with the characteristic structure of Type I isotherm [74]. The weak adsorption of hydrogen on Pt/Al_2O_3 catalyst was explained by the dual Langmuir model and it was shown that this model successfully represents the adsorption processes on homogeneous surfaces. In addition, the decrease in adsorption capacity with increasing temperature was consistent with the findings supporting the exothermal nature of the process [75]. In general, each isotherm model showed different levels of agreement depending on the physical–chemical structure of the adsorbent used and the experimental conditions.

3.4. Adsorption kinetics

In gas adsorption processes, the adsorption rate is an important parameter that determines how fast the gas can adhere to the adsorbent. This property is of great importance especially in areas where system efficiency and response time are critical, such as energy storage, separation and sensor applications. Therefore, in addition to high adsorption capacity, fast kinetic properties also play a vital role for an ideal adsorbent. Fig. 9 shows the changing of hydrogen gas adsorption amounts of P4, P6, P7, P8 and P9 at 40, 63 and 81 bar with time. In all samples, the adsorption process occurs rapidly at the beginning and a decrease in rate is observed over time as the equilibrium is reached; this situation is in accordance with classical gas–solid adsorption kinetics. As the pressure increases, the adsorption rate increases significantly and the time to reach equilibrium is shortened. Especially under 81 bar, a rapid adsorption onset is observed in all samples, which reveals that the surface interacts with more molecules in a short time at high pressure. P9 has the highest adsorption capacity and the fastest equilibrium time, which positions it as the adsorbent with the best kinetic performance. P7 and P8 also have high initial rates, while the final adsorption amounts are lower compared to P9. P4 exhibits relatively slow kinetics, reaching the saturation level later, especially at 40 bar. P6 exhibits a balanced kinetic behavior with a fast onset and medium saturation value. It is noteworthy that the adsorption curves reach saturation in a shorter time under high pressure in all samples and are similar to the Langmuir type kinetic model. The reaction rate reaches the highest level, especially in the 0–1 min range, which can be explained by the fast surface interactions of gas molecules. The slowdown following this rapid phase indicates that adsorption becomes diffusion controlled as the surface is filled. As a result, as the pressure increases, not only the total adsorption amount but also the adsorption rate increases. When evaluated in terms of kinetics, P9 stands out as the fastest and most effective adsorbent, while P4 exhibits the slowest kinetic behavior. These findings reveal that adsorbents should be evaluated not only in terms of capacity but also according to their kinetic performance.

Determination of the adsorption degree from adsorption rate data is a critical step for a better understanding of the adsorption mechanism. This analysis allows determining whether the process is physical or chemical adsorption, the type of surface interactions and the rate-determining step. In addition, the selecting the true kinetic model plays an important role in the design, scaling and process optimization stages. In the literature, pseudo-first-order, pseudo-second-order and Elovich equations are widely used in determining the adsorption degree [60,76]. The pseudo-first-order kinetic equation assumes that the adsorption rate is proportional to the amount of unadsorbed surface. This model is generally used to describe physical adsorption and is also known as the Lagergren model. The equation is expressed as follows:

$$\frac{dq_t}{dt} = k_1(q_e - q_t) \tag{9}$$

where q_t is the amount adsorbed at any time t (mmol/g), q_e is the amount adsorbed at equilibrium (mmol/g), and k_1 is the pseudo-first-order rate constant (1/min). When this equation is integrated, a linear expression is obtained as:

$$ln(q_e - q_t) = lnq_e - k_1 t \tag{10}$$

and kinetic parameters can be determined with experimental data using

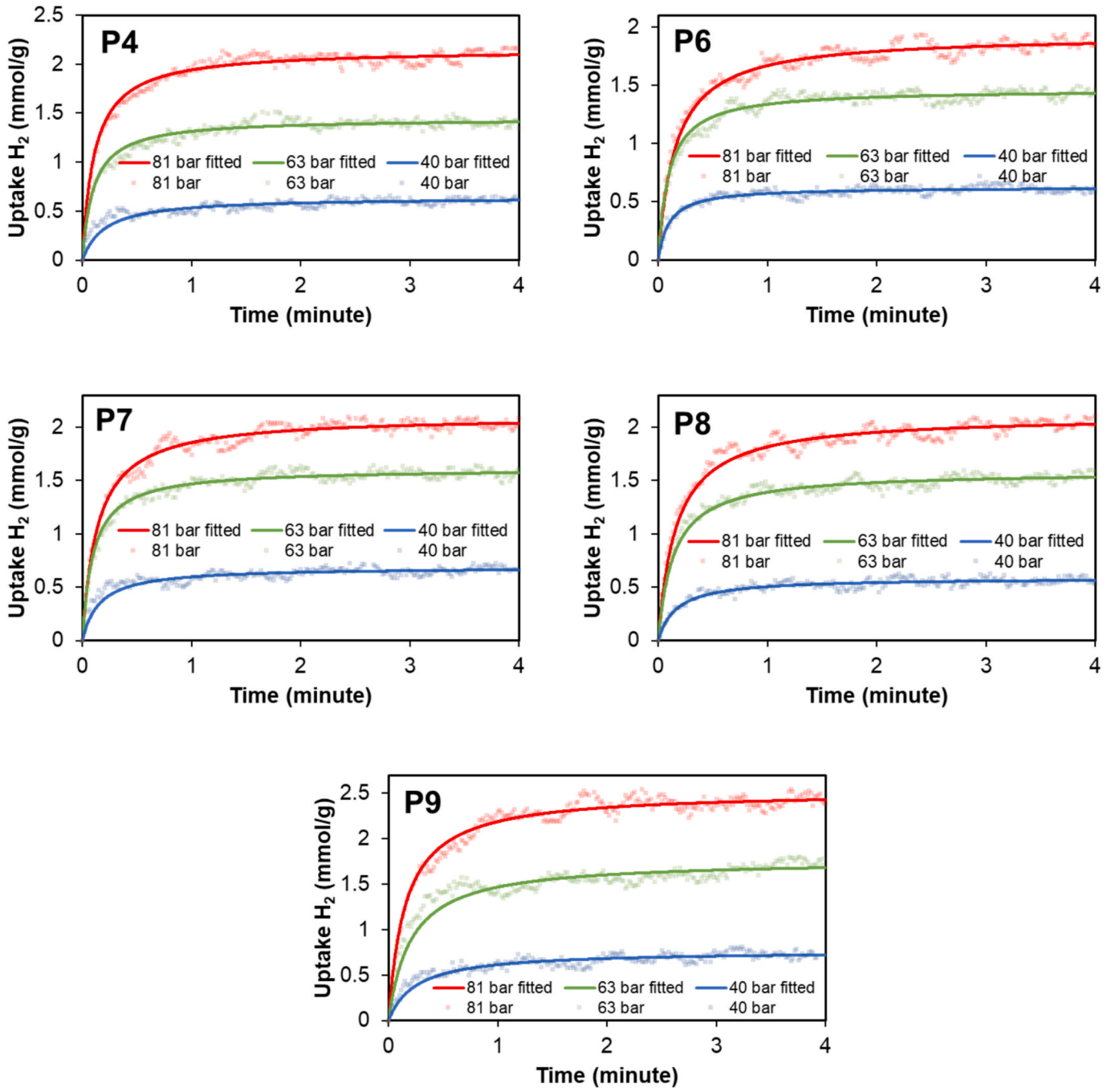

Fig. 9. The changing of adsorbed amounts with time for P4, P6, P7, P8 and P9 at different pressures.

this equation. The k_1 and q_e values can be calculated from the slope and extrapolation values of the ln(q_e-q_t) versus t plot, respectively [76].

The pseudo-second-order kinetic equation assumes that the adsorption rate is proportional to the square of the unadsorbed surface area and is generally used to describe chemical adsorption processes. Its differential form is as follows:

$$\frac{dq_t}{dt} = k_2(q_e - q_t)^2 \tag{11}$$

Where q_t is the amount of adsorbed substance at any time t (mmol/g), q_e is the amount of adsorption at equilibrium (mmol/g) and k_2 is the pseudo-second-order rate constant (g/mmol•min). When this equation is integrated, the following linear form is obtained:

$$\frac{t}{q_t} = \frac{1}{k_2 q_e^2} + \frac{t}{q_e} \tag{12}$$

In this equation, q_e and k_2 values can be calculated from the slope and estrapolation values of the plot of t/q_t against t, respectively [76].

The Elovich equation states that the reaction rate varies nonlinearly depending on the amount of adsorbed substance, especially in processes such as surface adsorption and chemical reactions. The equation is used to model different rate behaviors at low and high adsorption levels. The linear form of the equation can be given as follows:

$$q_t = \alpha ln t + \alpha ln(\alpha\beta) \tag{13}$$

In this equation, α is the initial adsorption rate and β is the desorption

Table 7
Kinetic parameters of cotton waste and biochar samples for hydrogen adsorption.

Samples	Pressures (bar)	Pseudo-first order, R^2	Pseudo-second order R^2	$q_{e(exp)}$ (mmol/g)	$q_{e(cal)}$ (mmol/g)	k_2	Elovich R^2	Boyd R^2	Weber-Morris R_1^2	k_1	R_2^2	k_2	Avrami R^2	n	k
P4	40	0.6876	0.9884	0.707	0.640	7.73	0.8421	0.5759	0.9471	0.803	0.6907	0.116	0.8002	0.324	1.364
	63	0.5059	0.9967	1.578	1.444	6.93	0.8575	0.4351	0.9321	1.776	0.5540	0.177	0.7861	0.351	1.558
	81	0.6090	0.9968	2.190	2.151	4.29	0.8494	0.4145	0.9474	2.458	0.4974	0.195	0.8136	0.441	1.965
P6	40	0.4519	0.9907	0.705	0.625	16.51	0.7534	0.3653	0.9382	0.833	0.3846	0.061	0.7225	0.343	1.513
	63	0.5245	0.9963	1.524	1.462	7.16	0.8100	0.3765	0.9804	1.970	0.4558	0.145	0.7538	0.397	1.855
	81	0.7007	0.9964	2.012	1.930	3.30	0.9004	0.5063	0.9556	2.109	0.6911	0.249	0.8502	0.411	1.594
P7	40	0.5671	0.9884	0.751	0.687	9.46	0.7826	0.4626	0.9147	0.928	0.5542	0.097	0.7248	0.328	1.520
	63	0.4808	0.9970	1.644	1.610	6.36	0.8372	0.4007	0.9758	2.193	0.5963	0.167	0.7857	0.426	2.038
	81	0.6534	0.9976	2.117	2.106	3.51	0.8840	0.4709	0.9465	2.342	0.6237	0.247	0.8316	0.481	1.897
P8	40	0.4669	0.9843	0.648	0.587	10.39	0.7927	0.4431	0.9646	0.755	0.4481	0.082	0.7684	0.419	1.414
	63	0.6849	0.9962	1.625	1.583	4.53	0.8639	0.4590	0.9746	2.219	0.6980	0.200	0.8364	0.407	1.792
	81	0.7557	0.9965	2.144	2.109	2.92	0.8834	0.4906	0.9687	2.359	0.7148	0.243	0.8545	0.439	1.736
P9	40	0.6287	0.9794	0.835	0.766	5.22	0.8463	0.5817	0.9450	0.913	0.6413	0.156	0.7964	0.394	1.249
	63	0.6325	0.9910	1.801	1.765	2.78	0.8608	0.5348	0.9782	2.263	0.7367	0.247	0.7750	0.409	1.659
	81	0.6047	0.9961	2.578	2.521	2.60	0.8881	0.4877	0.9470	2.671	0.5803	0.319	0.8526	0.474	1.707

constant. If the experimental data fit this equation, the plot of q_t against lnt should give a straight line with slope α and extrapolation αln(αβ). From the slope and extrapolation, α and β can be calculated [70].

The regression coefficient (R^2) values and related kinetic parameters obtained as a result of applying the experimental data to the pseudo-first-order, pseudo-second-order and Elovich equations are presented in Table 7. When the table is examined, it is observed that the R^2 values for P4, P6, P7, P8 and P9 are generally higher in the pseudo-second-

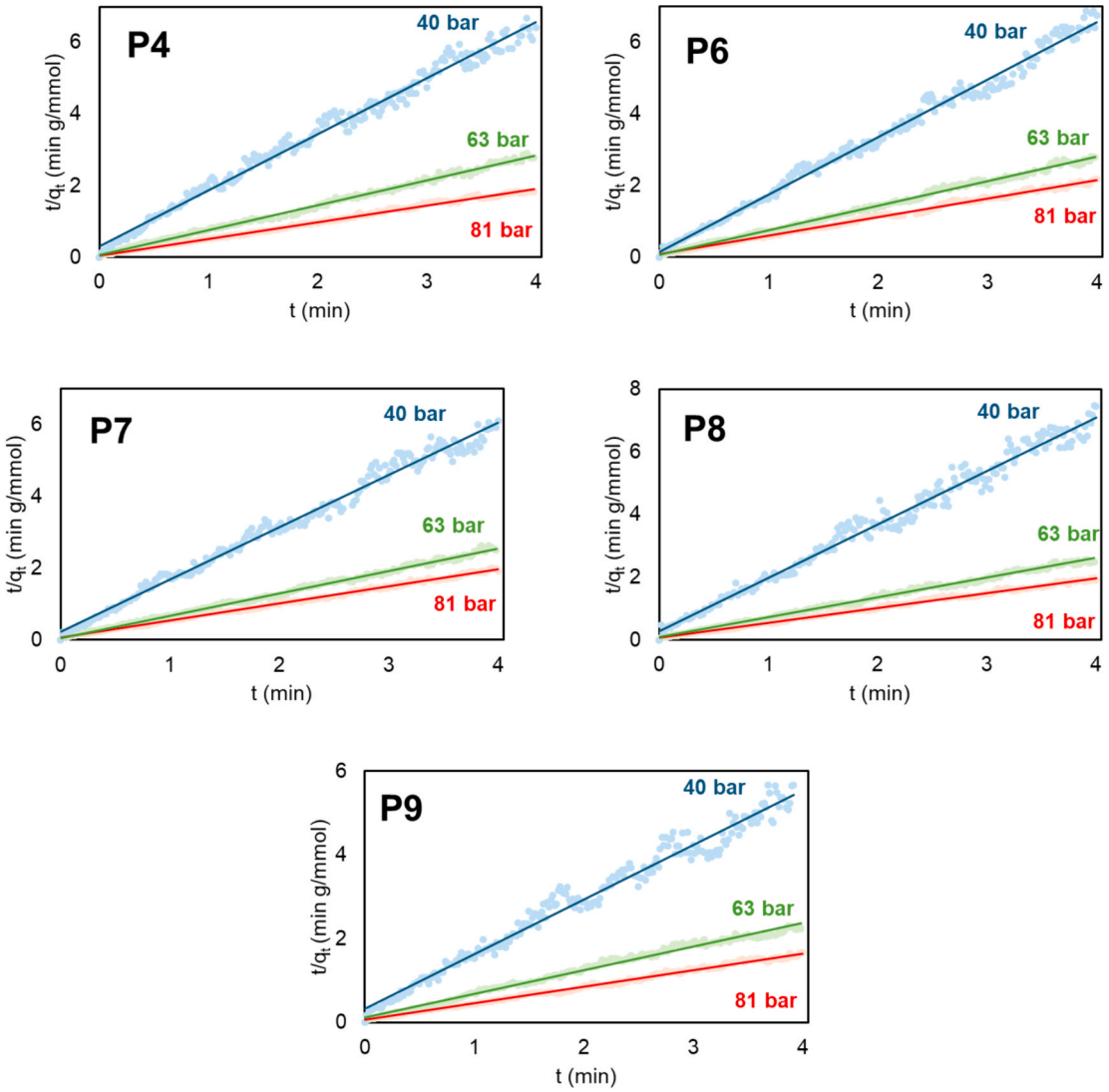

Fig. 10. The plots of t/q_t versus t for P4, P6, P7, P8 and P9 at different pressures.

order kinetic model. The R^2 values calculated for this model are mostly above 0.99, revealing that the experimental data show a strong fit to this kinetic model. On the other hand, the R^2 values of the pseudo-first-order model mostly remain at the level of 0.6, indicating that the model cannot adequately explain the data. Although high R^2 values are obtained in some samples based on the Elovich model, the general trend is in favor of the pseudo-second-order model. These findings show that the adsorption process is related to the filling of the active sites on the surface and that this mechanism significantly affects the adsorption dynamics. Comparison of $q_{e(cal)}$ and $q_{e(exp)}$ values given for the pseudo-second-order kinetic equation in Table 7 shows that both values are quite close to each other. This fit proves that the pseudo-second-order kinetic model successfully represents the experimental data. In order to evaluate the fit more clearly, the percentage error values for each pressure and sample can also be examined. For example, for P6 at 63 bar, $q_{e(exp)} = 1.524$ mmol/g and $q_{e(cal)} = 1.462$ mmol/g, in which case the percentage error is approximately 4.1 %. In P9, the percentage error is around 2.2 % at 81 bar; this can be considered as a very low deviation. When we examine the table, it is seen that the percentage error ratios mostly vary between 1 % and 9 %, and these ratios support the reliability of the model. Low error ratios show that the adsorption capacity is predicted correctly by the pseudo-second-order equation both numerically and statistically. As a result, both high R^2 values and low percentage error ratios reveal that the pseudo-second-order kinetic model best represents the adsorption behavior in this system. Moreover, it is clearly seen from Fig. 9 that the $q_{e(cal)}$ values calculated with the pseudo-second-order kinetic model show high agreement with the experimental data. Fig. 10 shows the curves of t/q_t versus t for P4, P6, P7, P8 and P9. In the studies examining the kinetics of hydrogen adsorption in the literature, it is emphasized that the adsorption mechanism varies in direct relation to the surface morphology, chemical structure and experimental parameters of the adsorbent material. For example, experimental studies conducted on organic-rich shale rocks have revealed that the pseudo-second-order kinetic model provides high agreement at low temperature and high pressure conditions [77]. This finding indicates that the adsorption rate is controlled by the chemical interactions between the active centers on the surface and hydrogen molecules. In theoretical comparisons made on $Mg_{17}Al_{12}$ and pure magnesium surfaces, it was determined that the alloy structure increased the adsorption capacity and accelerated the kinetic processes [78]. In adsorption–desorption experiments on the graphite surface, it was reported that the processes were reversible and the obtained kinetic data were compatible with the theoretical modeling [79]. In a study conducted by Doğan et al. (2025), it was found that the pseudo-second-order kinetic model in fullerene and defective fullerene structures showed a strong correlation with $R^2 > 0.99$ [6]. Similarly, Haidry et al. (2023) obtained high agreement with the pseudo-second-order kinetic model in $Pt/TiO_2/Pt$ based sensors and emphasized the reliability of this model in terms of sensor sensitivity [80]. In the study of Saied et al. (2025), it was reported that the adsorption process on Fe-modified hollow silica spheres (HSS) was limited by the chemical bonding with the active surface regions and that pseudo-second-order kinetics was valid in this context [81]. These studies show that a common kinetic behavior trend is exhibited in different material types and that this model is successful in explaining the general mechanism of hydrogen adsorption processes. As a result, the pseudo-second-order kinetic model stands out as an effective tool in the modeling and design of hydrogen storage systems with high correlation coefficients and low calculation errors.

Understanding the adsorption mechanisms on the biochar surface is of critical importance to increase hydrogen storage efficiency. Correct modeling of the adsorption process plays a fundamental role in increasing the capacity and efficiency of the adsorbent. In this context, Boyd, Weber-Morris and Avrami equations are frequently used to understand the adsorption mechanism of hydrogen on the biochar surface [82,83]. The Boyd equation is a model developed to investigate the dynamics of external mass transfer in adsorption processes. This equation mathematically expresses the transfer of gas molecules to the adsorbent surface and the mass transfer in this process. The Boyd equation is usually written in linear form as follows:

$$ln\left(1-\frac{q_t}{q_e}\right) = -0.497 - \frac{\pi^2 D_c}{r_c^2} t \tag{14}$$

In this equation, q_t is the amount adsorbed at any time t (mmol/g); q_e is the amount adsorbed at equilibrium (mmol/g); D_c is the diffusion coefficient (cm^2/min); r_c is the diameter of the adsorbent (cm); t is the time (min). If the curve of $\ln(1-q_t/q_e)$ against t passes through the origin, it can be said that the adsorption mechanism is intraparticle diffusion, and if it intersects the y-axis at −0.497, it can be said that it is external mass transfer [82].

The Avrami equation is another kinetic model used to explain the possible changes in the mechanisms that occur during the adsorption process. The Avrami equation can be written in linear form as follows:

$$ln[-ln(1-\theta)] = lnk + nlnt \tag{15}$$

In this equation, k is the kinetic constant; θ is the coverage fraction (q_t/q_e); n is a constant related to the adsorption mechanism. For the Avrami equation, if the plot of $\ln[-\ln(1-\theta)]$ against t passes through the origin and/or if the value of n is less than one, it can be said that the adsorption mechanism is diffusion controlled [83].

The Weber-Morris model describes diffusion processes, especially in the solid phase, and explains how the adsorption rate changes depending on the diffusion properties in the internal structure of the adsorbent. The Weber-Morris model can also be expressed in linear form:

$$q_t = k_{int}\sqrt{t} + C \tag{16}$$

In this equation, k_{int} is the intraparticle diffusion rate constant and C is a constant representing the intraparticle diffusion effect. This equation represents the initial fast interaction of adsorption and the adsorption rate slowing down over time [84].

The regression coefficients and related constants obtained by applying the experimental data to the Boyd, Avrami and Weber-Morris equations are presented in Table 7. When the table is examined, it is seen that the model that best fits the hydrogen adsorption mechanism on the biochar surface is the Weber-Morris equation. Especially, R_1^2 and R_2^2 values are above 0.90 in most samples and pressures, indicating that intraparticle diffusion plays an important role in the adsorption process. For example, in P8 and P9, very high R_1^2 values such as 0.9646, 0.9687 and 0.9450, 0.9470 were obtained at 63 and 81 bar, respectively. This suggests that intraparticle diffusion is a determining factor in the kinetic process. The R^2 values of the Boyd model vary from sample to sample and in some cases fall below 0.50 (e.g., 40 bar for P6: 0.3653), which reveals that external mass transfer alone cannot sufficiently explain the adsorption process. The Avrami model generally presents R^2 values in the range of 0.70–0.85, indicating that surface reactions have a limited effect. It is observed that the R^2 values of the Avrami model (in the range of 0.7248–0.8526) are lower than those of the Weber-Morris model, especially in P7 and P9. These findings reveal that hydrogen adsorption is not only a process that occurs on the surface, but also physical mass transfer mechanisms such as intra-pore diffusion play an important role. As a result, the Weber-Morris equation was evaluated as the most suitable model to explain the hydrogen adsorption process on the biochar surface. Fig. 11 shows the relationships between the adsorption amount (q_t) and the square root of time ($t^{0.5}$) in the graphs drawn according to the Weber–Morris model. When the data from Fig. 11 and Table 7 are evaluated together, it is understood that hydrogen adsorption occurs on the biochar surface by a two-stage diffusion mechanism. The q_t–$t^{0.5}$ curves obtained in all samples are characterized by two linear regions with different slopes. The first region of the curves with a steep slope at the beginning corresponds to the fast adsorption phase and this phase

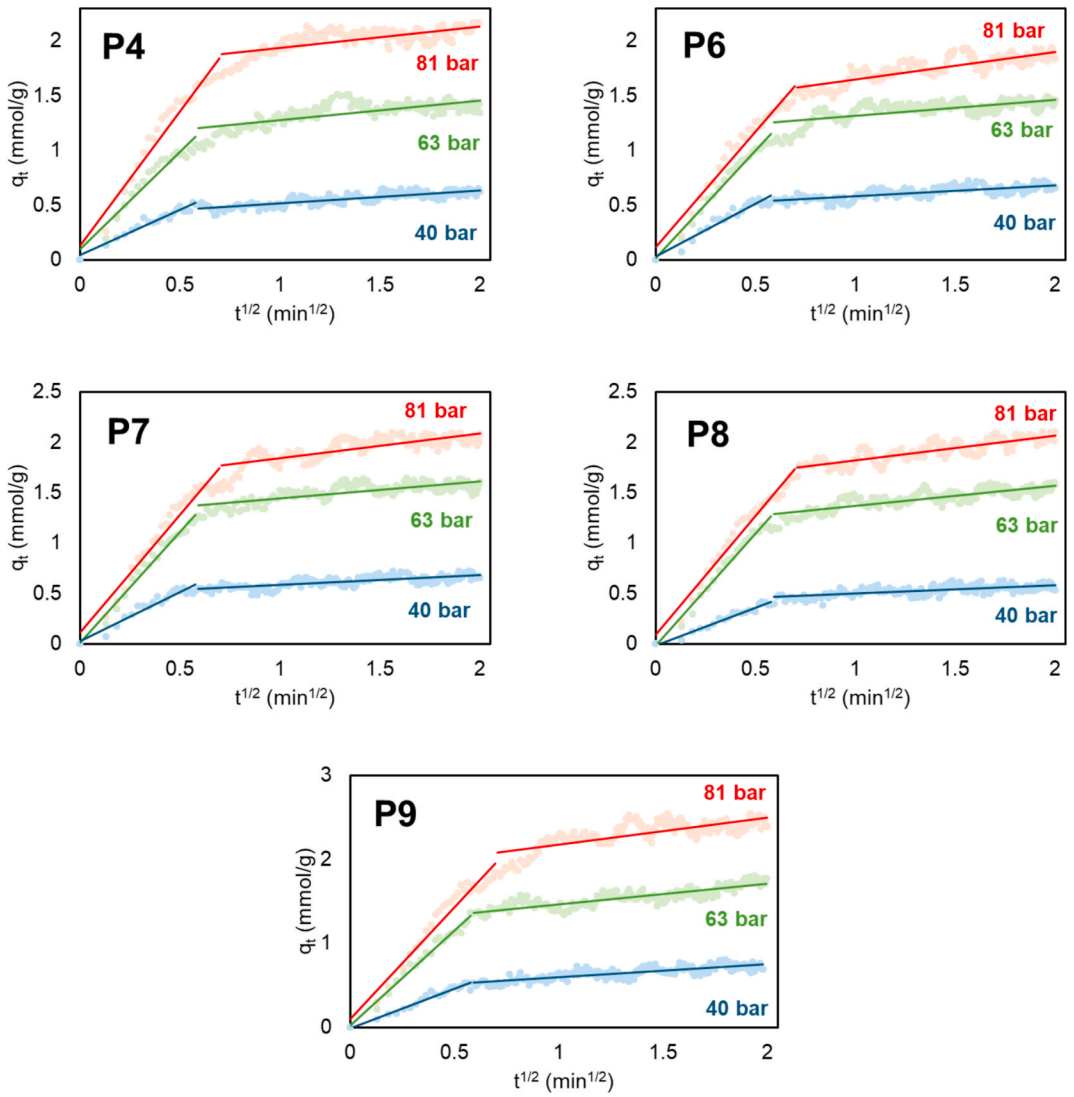

Fig. 11. The plots of q_t versus $t^{0.5}$ for P4, P6, P7, P8 and P9 at different pressures.

reflects the effect of the mesoporous structure. This linear region mostly passes through the origin or starts very close to the origin. The second linear region of the curve has a more horizontal slope and represents the slow internal diffusion phase towards the micropores. In this phase, the adsorption rate decreases significantly and the system approaches equilibrium over time. When the regression coefficients of the Weber–Morris model in Table 7 are examined, it is seen that the R_1^2 values of the first phase in particular are quite high (for example, 0.9646 at 63 bar for P8; 0.9687 at 63 bar for P9). These findings show that the model successfully describes the fast adsorption phase occurring in the mesopores. On the other hand, the R_2^2 values of the second phase are generally lower (e.g., 0.3846 at 40 bar for P6; 0.5803 at 81 bar for P9), indicating that microporous structures contain a more complex and slowly progressing diffusion process. Especially in the curves obtained under 81 bar, the separation between these two phases became quite clear. High pressure not only increases the adsorption capacity but also increases the observability of the second phase. The fact that both the first and second linear phases can be clearly distinguished in P6, P7 and P8 shows that these samples contain both meso- and microporous structures. The deviation of the curves from the origin in the figures shows that the surface interactions are completed at the beginning of the adsorption process and then a slow diffusion towards the inner structure starts. This confirms that intra-particle diffusion is the rate-determining step and that the adsorption is kinetically separated into two different stages. This transition can be observed quite clearly especially in P7 and P8 and is consistent with the data in Table 7. In P4, which has a lower adsorption capacity, the slope of the second phase is quite low; this shows that the micropore contribution is limited. The k_2 value supporting this situation is also quite low (for example, 0.1160 at 40 bar for P4). On the other hand, P9 has the highest k_1 (2.6710) and high R_1^2 (0.9470) values under 81 bar and has achieved rapid and effective adsorption in the first phase. As a result, both graphical and numerical analyses show that hydrogen adsorption occurs on biochar with a two-stage mechanism and this process is successfully represented by the Weber–Morris model. While the first phase of adsorption is faster and is shaped by the effect of mesopores, the second phase progresses in micropores with a slower and limited intraparticle diffusion.

3.5. Conclusions

This study aimed to evaluate cotton wastes with an environmentally friendly approach, convert them into high surface area biochars under different pyrolysis and activation conditions and to comprehensively investigate the hydrogen storage performances of these materials. Within the scope of the experimental design, parameters such as pyrolysis temperatures (300–800 °C), atmosphere types (N_2 and CO_2), KOH/biomass ratios (1:10 and 1:20) and CO_2 flow rates (25–100 mL/min) were systematically changed and a total of nine different biochar

samples were obtained. Characterization studies were carried out by BET, FTIR, DTA/TG and SEM/EDX analyses; thus, the structural, morphological and thermal properties of the materials were revealed in detail. TG/d[TG] analyses confirmed that pyrolysis effectively increased the fixed carbon content by eliminating volatile fractions, while high-temperature treatments (particularly in samples P4, P6 and P9) produced more thermally stable and structurally consolidated carbon frameworks. SEM images revealed that biochars had more developed and irregular porous structures after activation, while EDX analyses showed that activation in a CO_2 atmosphere increased the carbon/oxygen ratio and formed purer carbon structures. According to BET results, the highest surface area was obtained in P9 with 1446 m2/g, and parallel to this increase, a significant increase in micropore volume (0.570 cc/g) was observed. These properties directly contributed to the hydrogen adsorption capacity, especially at cryogenic temperatures. Hydrogen storage analyses showed that the storage capacity increased in samples with high surface area and micropore volume (especially P7–P9). At 77 K and 17.4 bar, P9 reached 2.79 wt% hydrogen storage capacity, presenting the highest value in the study. This value is above the theoretical limit predicted by Chahine's rule, indicating that performance can be optimized with pore structure. Adsorption isotherm analyses revealed that the Langmuir model provided the highest agreement ($R2 > 0.996$) in all samples and that the adsorption occurred as a monolayer on homogeneous surfaces. In addition, the fact that the differences between q_e and q_m values were less than 3 % showed that the model successfully represented the experimental data. Adsorption kinetic analyses revealed that rapid adsorption occurred at high pressures and the saturation state was reached in a short time, and P9 was the most successful material in terms of both capacity and rate. According to the kinetic modeling results, the adsorption processes showed a strong agreement with pseudo-second-order kinetics. In addition, the Weber–Morris model revealed that internal diffusion was an important but not the only rate-limiting step. These results show that the distribution of hydrogen in the adsorbent is controlled by multiple mechanisms. As a result of statistical analyses, strong positive correlations were found between the hydrogen storage capacity and BET surface area ($R = 0.87$) and micropore volume ($R = 0.86$); In addition, regression analyses confirmed that these relationships were statistically significant. All these findings indicate that cotton waste can be converted into high-performance adsorbents with appropriate activation conditions and that these materials are strong candidates for energy storage systems, especially hydrogen storage. In addition, such biochars offer sustainable, low-cost and environmentally friendly alternatives for fuel cells and other gas storage applications. Importantly, the results also demonstrate that the combined chemical (KOH) and physical (CO_2) activation strategy provides a more sustainable and superior route for producing high–surface–area carbons from cotton waste, while reducing the amount of corrosive KOH required—an outcome that represents the primary novelty and key contribution of this study.

CRediT authorship contribution statement

Mecit Karadaş: Software, Methodology, Investigation. **Gözde Duman:** Writing – original draft, Supervision, Methodology, Formal analysis, Data curation. **Mehmet Doğan:** Writing – review & editing, Writing – original draft, Visualization, Validation, Supervision, Software, Resources, Methodology, Formal analysis, Data curation, Conceptualization. **Yasemin Turhan:** Writing – original draft, Methodology, Data curation, Conceptualization. **Tamer Karayıldırım:** Methodology, Data curation, Conceptualization.

Declaration of competing interest

The authors declare that they have no known competing financial interests or personal relationships that could have appeared to influence the work reported in this paper.

Data availability

Data will be made available on request.

References

[1] Doğan EE, Tokcan P, Kızılduman BK. Storage of hydrogen in activated carbons and carbon nanotubes. Adv Mater Sci 2018;18:58. https://doi.org/10.1515/adms-2017-0045.

[2] Doğan EE. Hydrogen production and its storage from solar energy. Adv Mater Sci 2020;20:14–25. https://doi.org/10.2478/adms-2020-0007.

[3] Mulky L, Srivastava S, Lakshmi T, Sandadi ER, Gour S, Thomas NA, et al. An overview of hydrogen storage technologies – Key challenges and opportunities. Mater Chem Phys 2024;325:129710. https://doi.org/10.1016/j.matchemphys.2024.129710.

[4] Li H, Cao X, Liu Y, Shao Y, Nan Z, Teng L, et al. Safety of hydrogen storage and transportation: an overview on mechanisms, techniques, and challenges. Energy Rep 2022;8:6258–69. https://doi.org/10.1016/j.egyr.2022.04.067.

[5] Yalçınkaya FN, Doğan M, Bicil Z, Kızılduman BK. Effect of functionalization and Li-doping methods to hydrogen storage capacities of MWCNTs. Fuel 2024;372:132274. https://doi.org/10.1016/j.fuel.2024.132274.

[6] Doğan M, Kalafat MY, Kızılduman BK, Bicil Z, Turhan Y, Yanmaz E, et al. Hydrogen storage analysis of fullerene and defective fullerenes: the first experimental study. Fuel 2025;390:134705. https://doi.org/10.1016/j.fuel.2025.134705.

[7] Isinkaralar K, Gullu G, Turkyilmaz A, Doğan M, Turhan O. Activated carbon production from horse chestnut shells for hydrogen storage. Int J Glob Warming 2022;26:361–73. https://doi.org/10.1504/IJGW.2022.122430.

[8] Doğan ZS, Doğan EE, Bicil Z, Koçer KB. The effect of Li-doping and doping methods to hydrogen storage capacities of some carbonaceous materials. Fuel 2025;396:135280. https://doi.org/10.1016/j.fuel.2025.135280.

[9] Doğan M, Selek A, Turhan O, Kızılduman BK, Bicil Z. Different functional groups functionalized hexagonal boron nitride (h-BN) nanoparticles and multi-walled carbon nanotubes (MWCNT) for hydrogen storage. Fuel 2021;303:121335. https://doi.org/10.1016/j.fuel.2021.121335.

[10] Akasaka H, Takahata T, Toda I, Ono H, Ohshio S, Himeno S, et al. Hydrogen storage ability of porous carbon material fabricated from coffee bean wastes. Int J Hydrogen Energy 2011;36:580–5. https://doi.org/10.1016/j.ijhydene.2010.09.102.

[11] Kim W, Kim P, Joo JB, Shin HK, Jung KS, Yi J. The preparation and characterization of porous carbons for hydrogen storage. J Electroceram 2006;17:679–82. https://doi.org/10.1007/s10832-006-9712-8.

[12] Reddy KSK, Shoaibi AA, Srinivasakannan C. Preparation of porous carbon from date palm seeds and process optimization. Int J Environ Sci Technol 2015;12:959–66. https://doi.org/10.1007/s13762-013-0468-9.

[13] Haigler CH, Betancur L, Stiff MR, Tuttle JR. Cotton fiber: a powerful single-cell model for cell wall and cellulose research. Front Plant Sci 2012;3:104. https://doi.org/10.3389/fpls.2012.00104.

[14] Vijayakumar M, Santhosh R, Adduru J, Rao TN, Karthik M. Activated carbon fibres as high performance supercapacitor electrodes with commecial level mass loading. Carbon 2018;140:465–76. https://doi.org/10.1016/j.carbon.2018.08.052.

[15] Sevilla M, Fuertes AB. The production of carbon materials by hydrothermal carbonization of cellulose. Carbon 2009;47:2281–9. https://doi.org/10.1016/j.carbon.2009.04.026.

[16] Wang Q, Cheng X, Zhang YH. Biomorphous porous carbon prepared from cotton stalk. Appl Mech Mater 2013;253–255:871–4. https://doi.org/10.4028/www.scientific.net/AMM.253-255.871.

[17] Tian J, Zhang T, Talifu D, Abulizi A, Ji Y. Porous carbon materials derived from waste cotton stalk with ultra-high surface area for high performance supercapacitors. Mater Res Bull 2021;143:111457. https://doi.org/10.1016/j.materresbull.2021.111457.

[18] El-Hendawy ANA, Alexander AJ, Andrews RJ, Forrest G. Effects of activation schemes on porous, surface and thermal properties of activated carbons prepared from cotton stalks. J Anal Appl Pyrol 2008;82(2):272–8. https://doi.org/10.1016/j.jaap.2008.04.006.

[19] Ismailova MG. Influence of the carbonization conditions on the formation of the porous structure of activated carbon from cotton lignin. Prot Met Phys Chem 2009;45:212–5. https://doi.org/10.1134/S2070205109020154.

[20] Bedane A, Guo T, Shirani B, Xiao H. Textural characteristics of activated carbons prepared from agricultural residues – review. Can J Chem Eng 2023;101(12):6718–39. https://doi.org/10.1002/cjce.24960.

[21] Duman G. Preparation of novel porous carbon from hydrothermal pretreated textile wastes: Effects of textile type and activation agent on structural and adsorptive properties. J Water Process Eng 2021;43:102286. https://doi.org/10.1016/j.jwpe.2021.102286.

[22] Patel H, Weldekidan H, Mohanty A, Misra M. Effect of physicochemical activation on CO_2 adsorption of activated porous carbon derived from pine sawdust. Carbon Capture Sci Technol 2023;8:100128. https://doi.org/10.1016/j.ccst.2023.100128.

[23] Tag AT, Duman G, Ucar S, Yanik J. Effects of feedstock type and pyrolysis temperature on potential applications of biochar. J Anal Appl Pyrol 2016;120:200–6. https://doi.org/10.1016/j.jaap.2016.05.006.

[24] Çakır Ü, Kestel F, Koçer Kızılduman B, Bicil Z, Doğan M. Multi walled carbon nanotubes functionalized by hydroxyl and Schiff base and their hydrogen storage properties. Diam Relat Mater 2021;120:108604. https://doi.org/10.1016/j.diamond.2021.108604.

[25] Yang T, Lua AC. Characteristics of activated carbons prepared from pistachio-nut shells by physical activation. J Colloid Interface Sci 2003;267(2):408–17. https://doi.org/10.1016/S0021-9797(03)00689-1.

[26] Deng H, Li G, Yang H, Tang J, Tang J. Preparation of activated carbons from cotton stalk by microwave assisted KOH and K_2CO_3 activation. Chem Eng J 2010;163(3):373–81. https://doi.org/10.1016/j.cej.2010.08.019.

[27] Carrier M, Loppinet-Serani A, Denux D, Lasnier JM, Ham-Pichavant F, Cansell F, et al. Thermogravimetric analysis as a new method to determine the lignocellulosic composition of biomass. Biomass Bioenergy 2011;35:298–307. https://doi.org/10.1016/j.biombioe.2010.08.067.

[28] Fan F, Li H, Xu Y, Liu Y, Zheng Z, Kan H. Thermal behaviour of walnut shells by thermogravimetry with gas chromatography–mass spectrometry analysis. R Soc Open Sci 2018;5:180331. https://doi.org/10.1098/rsos.180331.

[29] Mureddu M, Dessì F, Orsini A, Ferrara F, Pettinau A. Air- and oxygen-blown characterization of coal and biomass by thermogravimetric analysis. Fuel 2018;212:626–37. https://doi.org/10.1016/j.fuel.2017.10.005.

[30] Reed AR, Williams PT. Thermal processing of biomass natural fibre wastes by pyrolysis. Int J Energy Res 2004;28(2):131–45. https://doi.org/10.1002/er.956.

[31] Parthasarathy P, Narayanan SK. Determination of kinetic parameters of biomass samples using thermogravimetric analysis. Environ Prog Sustain Energy 2014;33(1):256–66. https://doi.org/10.1002/ep.11763.

[32] Rodríguez-Reinoso F, Molina-Sabio M, González MT. The use of steam and CO_2 as activating agents in the preparation of activated carbons. Carbon 1995;33(1):15–23. https://doi.org/10.1016/0008-6223(94)00100-e.

[33] Georgieva V, Zvezdova D, Vlaev L. Non-isothermal kinetics of thermal degradation of chitosan. Chem Cent J 2012;6(1):81.

[34] Kok MV, Özgür E. Thermal analysis and kinetics of biomass samples. Fuel Process Technol 2013;106:739–43. https://doi.org/10.1016/j.fuproc.2012.10.010.

[35] Koçer Kızılduman B. Effect of fullerene (C70) on the structural, morphological optical and thermal properties of poly (butyl methacrylate)(PBMA). Fullerenes, Nanotubes, Carbon Nanostruct 2025;33(3):275–87. https://doi.org/10.1080/1536383X.2024.2416996.

[36] Kongkaew N, Pruksakit W, Patumsawad S. Thermogravimetric kinetic analysis of the pyrolysis of rice straw. Energy Procedia 2015;79:663–70. https://doi.org/10.1016/j.egypro.2015.11.552.

[37] Mahani NM, Oftadeh M. Kinetic and thermodynamic study of activated carbon from pistachio shell by thermogravimetric method. J Material Sci Eng A 2011;1(6A):887.

[38] Radić D, Stanojević M, Obradović M, Jovović A. Thermal analysis of physical and chemical changes occuring during regeneration of activated carbon. Therm Sci 2017;21(2):1067–81. https://doi.org/10.2298/TSCI150720048R.

[39] Song J, Jian WL, Wang L. Study on thermal Analysis Kinetics of Carbon support. Adv Mat Res 2013;750:1322–5. https://doi.org/10.4028/www.scientific.net/AMR.750-752.1322.

[40] Liu W, Yu J, Zhang J, Gao S, XuG. Kinetic study of reaction of porous solids. 2012. https://doi.org/10.1360/032011-833.

[41] Deng H, Zhang G, Xu X, Tao G, Dai J. Optimization of preparation of activated carbon from cotton stalk by microwave assisted phosphoric acid-chemical activation. J Hazard Mater 2010;182(1–3):217–24. https://doi.org/10.1016/j.jhazmat.2010.06.018.

[42] Wang M, Zhou D, Wang Y, Wei S, Yang W, Kuang M, et al. Bioethanol production from cotton stalk: a comparative study of various pretreatments. Fuel 2016;184:527–32. https://doi.org/10.1016/j.fuel.2016.07.061.

[43] Singh J, Bhunia H, Basu S. Adsorption of CO_2 on KOH activated carbon adsorbents: effect of different mass ratios. J Environ Manage 2019;250:109457. https://doi.org/10.1016/j.jenvman.2019.109457.

[44] Houache O, Al-Maamari R, Al-Rashidi B, Jibril B. Study of date palm stem as raw material in preparation of activated carbon. J Eng Res (TJER) 2008;5(1):47–54. https://doi.org/10.24200/tjer.vol5iss1pp47-54.

[45] Wu M, Guo Q, Fu G. Preparation and characteristics of medicinal activated carbon powders by CO_2 activation of peanut shells. Powder Technol 2013;247:188–96. https://doi.org/10.1016/j.powtec.2013.07.013.

[46] Song M, Jin B, Xiao R, Yang L, Wu Y, Zhong Z, et al. The comparison of two activation techniques to prepare activated carbon from corn cob. Biomass Bioenergy 2013;48:250–6. https://doi.org/10.1016/j.biombioe.2012.11.007.

[47] Fornes RE, Gilbert RD, Hersh SP, Dzubay TG. Energy-dispersive X-ray fluorescence analysis of dust collected using a vertical elutriator cotton dust sampler. Text Res J 1980;50(5):297–304. https://doi.org/10.1177/004051758005000506.

[48] Schenk ER, Almirall JR. Elemental analysis of cotton by laser-induced breakdown spectroscopy. Appl Opt 2010;49(13):C153. https://doi.org/10.1364/ao.49.00c153.

[49] Tsai WT, Jiang TJ. Mesoporous activated carbon produced from coconut shell using a single-step physical activation process. Biomass Convers Biorefin 2018;8:711–78. https://doi.org/10.1007/s13399-018-0322-x.

[50] Thommes M, Kaneko K, Neimark AV, Olivier JP, Rodriguez-Reinoso F, Rouquerol J, et al. Physisorption of gases, with special reference to the evaluation of surface area and pore size distribution (IUPAC Technical Report). Pure Appl Chem 2015;87(9–10):1051–69. https://doi.org/10.1515/pac-2014-1117.

[51] Demirbaş A. Biomass resource facilities and biomass conversion processing for fuels and chemicals. Energy Convers Manag 2001;42:1357–78. https://doi.org/10.1016/S0196-8904(00)00137-0.

[52] Chowdhury ZZ, Karim MZ, Ashraf MA, Khalid K. Influence of carbonization temperature on physicochemical properties of biochar derived from slow pyrolysis of durian wood (Durio zibethinus) sawdust. BioResources 2016;11(2):3356–72. https://doi.org/10.15376/biores.11.2.3356-3372.

[53] Keiluweit M, Nico PS, Johnson MG, Kleber M. Dynamic molecular structure of plant biomass-derived black carbon (biochar). Environ Sci Technol 2010;44:1247–53. https://doi.org/10.1021/es9031419.

[54] Yi Z, Li C, Li Q, Zhang L, Zhang S, Wang S, et al. Influence of CO_2 atmosphere on property of biochar from pyrolysis of cellulose. J Environ Chem Eng 2022;10:107339. https://doi.org/10.1016/j.jece.2022.107339.

[55] Valdés CF, Betancur Y, López D, Gómez CA, Chejne F. Effects of pyrolysis atmosphere on the porous structure and reactivity of chars from middle and high rank coals. Ing Investig 2017;38:1. https://doi.org/10.15446/ing.investig.v38n1.64516.

[56] Beyli PT, Doğan M, Bicil Z, Turhan Y, Yanmaz E, Kizilduman BK. Hydrogen Storage Performance of Sunflower Stalk-Derived Activated Carbons Produced via ZnCl2 and KOH Activation. Energy Storage 2025;7(6):70260. https://doi.org/10.1002/est2.70260.

[57] Turkyilmaz A, Isinkaralar K, Doğan M, Kızılduman BK, Bicil Z. Production, characterization, and hydrogen storage properties of activated carbon from horse chestnut shell. Sustain Chem Pharm 2024;40:101634. https://doi.org/10.1016/j.scp.2024.101634.

[58] Doğan M, Sabaz P, Bicil Z, Koçer Kızılduman B, Turhan Y. Activated carbon synthesis from tangerine peel and its use in hydrogen storage. J Energy Inst 2020;93:2176–85. https://doi.org/10.1016/j.joei.2020.05.011.

[59] Bag O, Tekin K, Karagoz S. Microporous activated carbons from lignocellulosic biomass by KOH activation. Fuller Nanotub Carbon Nanostruct 2020;28:12. https://doi.org/10.1080/1536383X.2020.1794850.

[60] Benard P, Chahine R. Determination of the adsorption isotherms of hydrogen on activated carbons above the critical temperature of the adsorbate over wide temperature and pressure ranges. Langmuir 2001;17:6. https://doi.org/10.1021/la001381x.

[61] Akgül A, Akın ŞŞ, Güleç F, Kazanç F. Biochar gasification: Insights from pyrolysis atmospheres and gasification heating rates. Fuel 2024;360:130469. https://doi.org/10.1016/j.fuel.2023.130469.

[62] Premchand P, Demichelis F, Chiaramonti D, Bensaid S, Fino D. Study on the effects of carbon dioxide atmosphere on the production of biochar derived from slow pyrolysis of organic agro-urban waste. Waste Manag 2023;172:308–19. https://doi.org/10.1016/j.wasman.2023.10.035.

[63] Ofuani N, Bhoi P. Carbon dioxide gasification of biochar: a sustainable way of utilizing captured CO_2 to mitigate greenhouse gas emission. Sustainability 2024;16:5044. https://doi.org/10.3390/su16125044.

[64] Wang J, Senkovska I, Kaskel S, Liu Q. Chemically activated fungi-based porous carbons for hydrogen storage. Carbon 2014;75:372–80. https://doi.org/10.1016/j.carbon.2014.04.016.

[65] Xia K, Gao Q, Song S, Wu C, Jiang J, Hu J, et al. CO_2 activation of ordered porous carbon CMK-1 for hydrogen storage. Int J Hydrogen Energy 2008;33:116–23. https://doi.org/10.1016/j.ijhydene.2007.08.019.

[66] Sun Y, Webley PA. Preparation of activated carbons from corncob with large specific surface area by a variety of chemical activators and their application in gas storage. Chem Eng J 2010;162:883–92. https://doi.org/10.1016/j.cej.2010.06.031.

[67] Lionetti V, Desiderio G, Bartucci S, Bonaventura CP, Policicchio A, Conte G, et al. Optimized activation of coffee-ground carbons for hydrogen storage. Int J Hydrogen Energy 2025;136:1029–40. https://doi.org/10.1016/j.ijhydene.2025.03.188.

[68] Turhan Y, Yeşilbiçer MB, Kizilduman BK, Doğan M, Bicil Y. Cryogenic hydrogen storage on peanut shell-derived-activated carbons: Isotherm, kinetics and mechanism. J Storage Mater 2025;140(Part A):118998. https://doi.org/10.1016/j.est.2025.118998.

[69] Kızılduman BK, Turhan Y, Doğan M. Mesoporous carbon spheres produced by hydrothermal carbonization from rice husk: Optimization, characterization and hydrogen storage. Adv Powder Technol 2021;32:4222–34. https://doi.org/10.1209/0295-5075/96/27013.

[70] Bicil Z, Doğan M. Characterization of activated carbons prepared from almond shells and their hydrogen storage properties. Energy Fuels 2021;35:10227–40. https://doi.org/10.1021/acs.energyfuels.1c00795.

[71] Hwang KS, Gong SY, Lee WK. Adsorption equilibria for hydrogen and carbon dioxide on activated carbon at high pressure up to 30 atm. Korean J Chem Eng 1991;8:148–55. https://doi.org/10.1007/BF02706676.

[72] Saha D, Wei Z, Deng S. Equilibrium, kinetics and enthalpy of hydrogen adsorption in MOF-177. Int J Hydrogen Energy 2008;33:7479–88. https://doi.org/10.1016/j.ijhydene.2008.09.053.

[73] Akyalcin S, Akyalcin L, Ertugrul E. Modification of natural clinoptilolite zeolite to enhance its hydrogen adsorption capacity. Res Chem Intermed 2024;50:1455–73. https://doi.org/10.1007/s11164-023-05212-2.

[74] Zhao XB, Xiao B, Fletcher AJ, Thomas KM. Hydrogen adsorption on functionalized nanoporous activated carbons. J Phys Chem B 2005;109:8880–8. https://doi.org/10.1021/jp050080z.

[75] Primet M, Basset JM, Mathieu MV. Infra-red determination of the isotherm of hydrogen adsorption on a Pt/Al_2O_3 catalyst. J Chem Soc Faraday Trans 1974;1(70):293–8. https://doi.org/10.1039/F19747000293.

[76] Alkan M, Demirbaş Ö, Doğan M. Adsorption kinetics and thermodynamics of an anionic dye onto sepiolite. Microporous Mesoporous Mater 2007;101(3):388–96. https://doi.org/10.1016/j.micromeso.2006.12.007.

[77] Alanazi A, Abid HR, Abu-Mahfouz IS, Bawazeer SA, Matamba T, Keshavarz A, et al. Hydrogen adsorption kinetics in organic-rich shale reservoir rocks for seasonal geological storage. Fuel 2025;379:132964. https://doi.org/10.1016/j.fuel.2024.132964.

[78] Zhou X, Yan X, He C, Yang XB, Zhao YJ. Theoretical study of hydrogen adsorption kinetics: $Mg_{17}Al_{12}$ vs pure Mg. Int J Hydrogen Energy 2023;48:18375–84. https://doi.org/10.1016/j.ijhydene.2023.01.273.
[79] Simon JM, da Silva GCQ. Adsorption kinetics model of hydrogen on graphite. Entropy 2025;27:229. https://doi.org/10.3390/e27030229.
[80] Haidry AA, Ji Y, Raza A, Zhu H, Zavabet A, Saruhan B. Elucidating the hydrogen adsorption kinetics on $Pt/TiO_2/Pt$ based highly efficient sensors. Mater Res Bull 2023;167:112415. https://doi.org/10.1016/j.materresbull.2023.112415.
[81] Saeid MF, Abdulkadir BA, Setiabudi HD. Enhancing hydrogen adsorption performance of hollow silica spheres through the addition of Fe: a study on kinetic and thermodynamic. Mater Sci Semicond Process 2025;192:109458. https://doi.org/10.1016/j.mssp.2025.109458.
[82] Saha D, Wei Z, Deng S. Hydrogen adsorption equilibrium and kinetics in metal–organic framework (MOF-5) synthesized with DEF approach. Sep Purif Technol 2009;64:280–7. https://doi.org/10.1016/j.seppur.2008.10.022.
[83] Doğan M, Turhan Y, Kızılduman BK, Turan Beyli P, Doğan S. Isothermal calcination kinetics of boric acid and its use for nano boron oxide production under cryogenic conditions. Inorg Nano-Met Chem 2024:1–10. https://doi.org/10.1080/24701556.2024.2356039.
[84] Doğan M, Alkan M, Türkyilmaz A, Özdemir Y. Kinetics and mechanism of removal of methylene blue by adsorption onto perlite. J Hazard Mater 2004;109(1–3):141–8. https://doi.org/10.1016/j.jhazmat.2004.03.003.